POLITECNICO DI TORINO
Repository ISTITUZIONALE

Hygro-electro-elastic analysis of plates and shells via a three-dimensional layer-wise exponential matrix formulation

Original
Hygro-electro-elastic analysis of plates and shells via a three-dimensional layer-wise exponential matrix formulation / Brischetto, S., Cesare, D.. - In: JOURNAL OF MECHANICS. - ISSN 1727-7191. - 42:(2026), pp. 387-410. [10.1093/jom/ufag025]

Availability:
This version is available at: 11583/3016190 since: 2026-10-01T08:24:20Z

Publisher:
Oxford University Press

Published
DOI:10.1093/jom/ufag025

Terms of use:

This article is made available under terms and conditions as specified in the corresponding bibliographic description in the repository

Publisher copyright

(Article begins on next page)

26 October 2026

Journal of Mechanics, 2026, 42, 387–410
https://doi.org/10.1093/jom/ufag025
Regular Article

OXFORD

Hygro–electro–elastic analysis of plates and shells via a three-dimensional layer-wise exponential matrix formulation

S. Brischetto* and D. Cesare

Department of Mechanical and Aerospace Engineering, Politecnico di Torino, Torino, Italy

*Corresponding author: salvatore.brischetto@polito.it

Abstract

A fully coupled hygro–electro–elastic (HEE) formulation is developed to investigate the static response of smart plate and shell structures for aerospace applications. The proposed three-dimensional model is based on a system of five coupled second-order differential equations expressed in the orthogonal mixed curvilinear coordinate system (α, β, z). Owing to a unified mathematical framework, spherical shells, cylindrical panels, cylinders, and flat plates can be analyzed under combined hygroscopic, electrical, and mechanical loadings. Simpler geometries are naturally recovered from the general spherical-shell formulation through appropriate assumptions on the curvature radii. The solution strategy combines Navier harmonic expansions along the in-plane directions with the exponential matrix technique through the thickness coordinate, leading to a closed-form three-dimensional solution. The formulation enables the direct evaluation of displacement and stress fields together with moisture content, moisture flux, electric potential, and electric displacement distributions. A layer-wise description is adopted across the thickness, ensuring an accurate representation of local three-dimensional effects for different thickness ratios and stacking sequences while preserving high computational efficiency. The accuracy of the proposed model is first assessed through comparisons with refined two-dimensional coupled HEE formulations available in the literature. Subsequently, a series of benchmark problems involving four structural geometries and three loading scenarios is presented to examine the static HEE behavior of curved smart structures and to highlight the influence of geometry, coupling effects, and loading conditions on the global and local responses. The proposed formulation investigates the mutual interaction among hygrometric, electrical, and mechanical fields in multilayered smart structures subjected to combined environmental and mechanical loading. Such coupling is relevant to aerospace smart structures employing *electrically* active materials, where moisture diffusion can modify the mechanical response and, consequently, the structural performance under environmental conditions.

Keywords: hgro–electro–elastic interaction, three-dimensional shell formulation, multilayered smart structures, layer-wise description, exact strong-form solution, exponential matrix technique

1. Introduction

Aerospace components are commonly manufactured as multilayered assemblies obtained by stacking several laminae according to a prescribed lay-up sequence. Such structural configurations have been extensively studied in the scientific literature with reference to bending behavior, fatigue phenomena, delamination mechanisms, and vibration characteristics. When hygrometric effects are considered, conventional multilayered aerospace structures may experience severe degradation processes. Moisture can diffuse into the material microstructure, promoting the deterioration of material properties and facilitating the onset of delamination. Understanding these phenomena, especially when combined with other interacting physical fields, is essential for the development of future aerospace structures. As a consequence, the traditional design philosophy based solely on resistance to mechanical loads during service conditions is progressively evolving toward a multifield-oriented approach. Within this context, the hygrometric field becomes particularly relevant because aircraft, unmanned aerial vehicles, and spacecraft are routinely exposed to environments characterized by variable humidity levels. Therefore, the multifield design of advanced multilay-

Received: 3 July 2026. **Revised:** 22 August 2026. **Accepted:** 10 September 2026
© The Author(s) 2026. Published by Oxford University Press on behalf of Society of Theoretical and Applied Mechanics of the Republic of China, Taiwan. This is an Open Access article distributed under the terms of the Creative Commons Attribution License (https://creativecommons.org/licenses/by/4.0/), which permits unrestricted reuse, distribution, and reproduction in any medium, provided the original work is properly cited.

Downloaded from academic.oup.com/jom/article/doi/10.1093/jom/ufag025/8845483 by Politecnico di Torino user on 30 September 2026

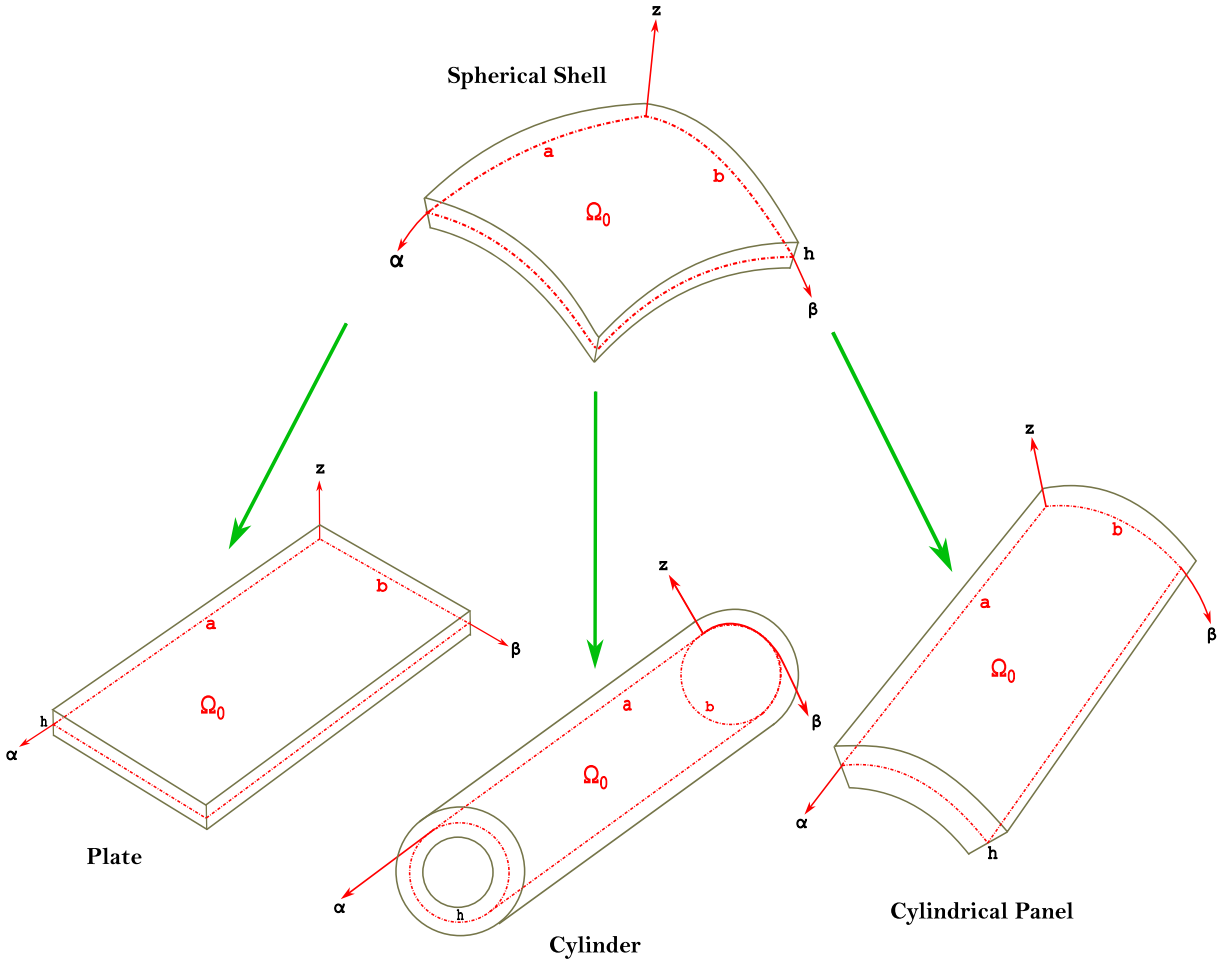

Figure 1 Geometries, mixed curvilinear orthogonal reference system and middle reference surfaces Ω_0 for assessments and benchmarks. Dotted lines indicates the middle reference surface Ω_0. The origin of the mixed curvilinear orthogonal reference system is indicated at the top left corner of each geometry. Spherical shell degenerates in simpler geometries.

ered aerospace structures requires the hygrometric field to be investigated together with the other conventional physical fields, namely thermal, electric, magnetic, and elastic ones.

The interaction between hygrometric effects and elastic and/or thermal fields has attracted considerable attention over the years. Among the various multifield problems, the hygro−elastic response of multilayered structures represents one of the most fundamental cases. Brischetto *et al.* [1, 2] introduced a three-dimensional formulation, available in both coupled and uncoupled forms, for multilayered and functionally graded spherical shells. Their model enables the evaluation of three-dimensional hygro−elastic phenomena in advanced layered structures. Brauns and Rocers [3] examined, for the first time, the influence of moisture on wood-based composite materials. Huč *et al.* [4] carried out a hygro−mechanical investigation of wooden specimens subjected to mechanical actions and different relative humidity conditions with the aim of predicting their long-term rheological response. Moisture diffusion in polymer-matrix composites reinforced with unidirectional fibers was analyzed by Jain and Mukherjee [5]. Nguedjio *et al.* [6] explored the effects of moisture-content gradients on the mechanical behavior of wood. Ožbolt *et al.* [7] investigated the relationship between load-induced damage in concrete and time-dependent nonelastic deformations through a three-dimensional meso-scale finite element framework. In [8], a coupled moisture–displacement finite element formulation was proposed to describe the viscoelastic mechano-sorptive response and the swelling/shrinkage behavior of timber components reinforced with fibers and subjected simultaneously to long-term loading and variations in relative humidity. Steinbrecher *et al.* [9] analyzed the role of hygro−mechanical coupling in the interlaminar failure of graphite–phenolic laminates. Wang and Cui [10] proposed a hygro−mechanical formulation for hollow glass bead/resin composites based on Fick's second diffusion law and validated the model through experimental observations.

It is well established that hygrometric and thermal fields are inherently interconnected, since temperature variations influence humidity levels and, conversely, humidity changes may affect thermal conditions. Consequently, hygro−thermo−elastic formulations play a significant role in the bending analysis of advanced structures. Ali *et al.* [11] examined the combined influence of moisture and tempera-

Downloaded from academic.oup.com/jom/article/doi/10.1093/jom/ufag025/8845483 by Politecnico di Torino user on 30 September 2026

Table 1 Material data in terms of elastic, hygrometric, and electric properties employed in the two proposed assessments (A1 and A2).

	Adaptive wood [51]	Soft adaptive wood [51]
	Elastic properties	
E_1 [GPa]	154.32	77.16
E_2 [GPa]	154.32	77.16
E_3 [GPa]	142.83	71.415
ν_{12} [-]	0.36564	0.18282
ν_{13} [-]	0.40133	0.200665
ν_{23} [-]	0.40133	0.200665
G_{12} [GPa]	56.5	28.25
G_{13} [GPa]	45.3	22.65
G_{23} [GPa]	45.3	22.65
	Hygrometric properties	
η_{11} $[10^{-4}\,m^3/kg]$	1.10	1.10
η_{22} $[10^{-4}\,m^3/kg]$	1.10	1.10
η_{33} $[10^{-4}\,m^3/kg]$	1.10	1.10
D_1 $[10^{-10}\,m^2]$	1.78	0.89
D_2 $[10^{-10}\,m^2]$	1.78	0.89
D_3 $[10^{-10}\,m^2]$	1.78	0.89
	Electric properties	
e_{15} $[C/m^2]$	11.6	5.8
e_{24} $[C/m^2]$	11.6	5.8
e_{31} $[C/m^2]$	−4.4	−2.2
e_{32} $[C/m^2]$	−4.4	−2.2
e_{33} $[C/m^2]$	18.6	9.3
ϵ_1 $[nF/m]$	0.08	0.04
ϵ_2 $[nF/m]$	0.08	0.04
ϵ_3 $[nF/m]$	0.0930	0.0465
s_3 $[Cm/kg]$	0	0

Table 2 Geometrical data and loading boundary conditions for the Assessment 1 (A1) and the Assessment 2 (A2).

	A1	A2
	Geometrical data	
a $[m]$	2	$\frac{1}{6}\pi R_\alpha$
b $[m]$	1	$\frac{2}{9}\pi R_\beta$
$R_\alpha[m]$	∞	3
$R_\beta[m]$	∞	3
h $[m]$	0.1	0.1
	Loading boundary conditions	
$\bar{P}_{z_t}[Pa]$	$-7\cdot10^5$	$-7\cdot10^5$
$\bar{P}_{z_b}[Pa]$	$3\cdot10^5$	$3\cdot10^5$
$\bar{\Phi}_t[A]$	$5\cdot10^4$	$5\cdot10^4$
$\bar{\Phi}_b[A]$	$5\cdot10^3$	$1\cdot10^4$
$\bar{\mathcal{M}}_t[kg/m^3]$	$5\cdot10^{-2}$	$8\cdot10^{-1}$
$\bar{\mathcal{M}}_b[kg/m^3]$	$2\cdot10^{-2}$	$6\cdot10^{-1}$
m	1	1
n	1	1

Overbar applied to maximum amplitudes means prescribed value. t and b mean top and bottom of the structure, respectively.

Table 3 Assessment A1, simply-supported three-layered *Adaptive Wood/Soft Adaptive Wood/Adaptive Wood* plate.

		ELDZL4 [51]	3D-u-$\mathcal{M}$-ϕ
u $[10^{-5}\,m]$	$(\tilde{z}/h=0.00)$	−1.10	−1.06
v $[10^{-5}\,m]$	$(\tilde{z}/h=0.50)$	−0.50	−0.50
w $[10^{-4}\,m]$	$(\tilde{z}/h=1.00)$	−1.22	−1.18
ϕ $[10^4\,A]$	$(\tilde{z}/h=0.30)$	−1.14	−1.20
$\mathcal{M}$ $[kg/m^3]$	$(\tilde{z}/h=0.50)$	0.017	0.017
σ_{zz} $[10^5\,Pa]$	$(\tilde{z}/h=0.50)$	−1.10	−1.11
$\mathcal{D}_\alpha$ $[10^{-4}\,C/m^2]$	$(\tilde{z}/h=0.50)$	−2.15	−2.14
$\mathcal{D}_\beta$ $[10^{-4}\,C/m^2]$	$(\tilde{z}/h=0.90)$	−3.26	−3.25

Results are considered in the in-plane point (0.25a, 0.25b) and in specified thickness locations $\tilde{z}/h$. $\tilde{z}/h$ goes from 0 (bottom) to 1 (top).

Table 4 Assessment A2, simply-supported three-layered *Adaptive Wood/Soft Adaptive Wood/Adaptive Wood* spherical shell.

		ELDZL4 [51]	3D-u-$\mathcal{M}$-ϕ
u $[10^{-5}\,m]$	$(\tilde{z}/h=0.00)$	−5.00	−4.70
v $[10^{-5}\,m]$	$(\tilde{z}/h=0.50)$	−3.00	−2.88
w $[10^{-4}\,m]$	$(\tilde{z}/h=1.00)$	−1.11	−0.98
$\mathcal{M}$ $[kg/m^3]$	$(\tilde{z}/h=0.50)$	0.348	0.348
$\mathcal{E}_\alpha$ $[10^4\,V/m]$	$(\tilde{z}/h=1.00)$	−4.92	−4.92
$\mathcal{E}_\beta$ $[10^4\,V/m]$	$(\tilde{z}/h=0.00)$	−0.76	−0.76
$\sigma_{\alpha z}$ $[10^5\,Pa]$	$(\tilde{z}/h=0.70)$	−6.18	−6.73

Results are considered in the in-plane point (0.25a, 0.25b) and in specified thickness locations $\tilde{z}/h$. $\tilde{z}/h$ goes from 0 (bottom) to 1 (top).

ture on the bending response of simply supported orthotropic cylindrical shells. Hirwani *et al.* [12] addressed the nonlinear time-dependent deflection behavior of delaminated composite shell panels subjected to hygro−thermo−mechanical loadings. Jouneghani *et al.* [13] investigated the bending performance of functionally graded nanobeams with internal porosity under combined hygro−thermo−mechanical actions. Kundu and Han [14] analyzed buckling phenomena and dynamic instabilities induced by hygrothermal stresses resulting from environmental variations. The aeroelastic response of smart composite plates operating in hygrothermal environments and subjected to aerodynamic loads was studied by Mahato and Maiti [15]. Moleiro *et al.* [16, 17] proposed a coupled layerwise mixed formulation for the static hygro−thermo−mechanical analysis of multilayered and functionally graded plates exposed to multifield loading conditions. Monge *et al.* [18] presented a three-dimensional bending solution for doubly-curved shells under mechanical and hygrothermal loads by incorporating both Fourier's heat conduction equation and Fick's moisture diffusion law. Penna *et al.* [19] investigated the dynamic behavior of porous functionally graded Bernoulli–Euler nanobeams in hygrothermal environments through the local/nonlocal stress gradient elasticity theory. Pham *et al.* [20–22] presented vibration and static analyses of functionally graded porous nanobeams, sandwich nanoshells, and curved beams by employing analytical formulations based

Downloaded from academic.oup.com/jom/article/doi/10.1093/jom/ufag025/8845483 by Politecnico di Torino user on 30 September 2026

Table 5 Elastic, hygrometric, and electric properties for material used in the new benchmarks B1, B2, B3, and B4.

	HEE material [38]
	Elastic properties
E_1 [GPa]	42.785
E_2 [GPa]	42.785
E_3 [GPa]	57.707
ν_{12} [-]	0.4805
ν_{13} [-]	0.2442
ν_{23} [-]	0.2442
G_{12} [GPa]	14.450
G_{13} [GPa]	13.200
G_{23} [GPa]	13.200
	Hygrometric properties
$\eta_{11}[10^{-4}\,m^3/kg]$	0.8
$\eta_{22}[10^{-4}\,m^3/kg]$	0.8
$\eta_{33}[10^{-4}\,m^3/kg]$	1.1
$D_1[10^{-5}\,m^2]$	18.5
$D_2[10^{-5}\,m^2]$	18.5
$D_3[10^{-5}\,m^2]$	18
	Electric properties
$e_{15}[C/m^2]$	−0.138
$e_{24}[C/m^2]$	−0.138
$e_{31}[C/m^2]$	−0.16
$e_{32}[C/m^2]$	−0.16
$e_{33}[C/m^2]$	0.347
$\epsilon_1[nF/m]$	0.0826
$\epsilon_2[nF/m]$	0.0826
$\epsilon_3[nF/m]$	0.0903
$s_3\,[10^{-5}\,Cm/kg]$	−2.5

Table 6 Geometrical data and half-wave numbers for the four new benchmarks (B).

	B1	B2	B3	B4
a [m]	2	$2\pi R_\alpha$	$\frac{\pi}{3}R_\alpha$	$\frac{\pi}{3}R_\alpha$
b [m]	1	10	10	$\frac{\pi}{3}R_\alpha$
R_α [m]	∞	10	10	10
R_β [m]	∞	∞	∞	10
m	1	2	1	1
n	1	1	0	1

Table 7 Benchmark B1, simply-supported multilayered rectangular plate in actuator configuration ($\bar{P}_{z_t} = 0\,Pa$, $\bar{P}_{z_b} = 0\,Pa$, $\bar{\Phi}_t = 1\cdot 10^8\,A$, $\bar{\Phi}_b = 0\,A$, $\bar{\mathcal{M}}_t = 1.5\,kg/m^3$, $\bar{\mathcal{M}}_b = 0.5\,kg/m^3$).

a/h	2	4	10	50	100
		$u\,[10^{-5}\,m]$ $(\tilde{z}/h = 0.00)$			
	7.0297	0.1495	−29.564	−183.93	−369.70
		$w\,[10^{-4}\,m]$ $(\tilde{z}/h = 0.75)$			
	3.0586	4.7426	6.3016	8.5132	10.919
		$\phi\,[10^6\,A]$ $(\tilde{z}/h = 0.25)$			
	6.6535	16.911	23.380	24.932	24.983
		$\mathcal{M}\,[kg/m^3]$ $(\tilde{z}/h = 0.25)$			
	0.2908	0.5463	0.7086	0.7483	0.7496
		$\sigma_{\alpha\beta}\,[10^7\,Pa]$ $(\tilde{z}/h = 0.75)$			
	−1.3384	−1.9699	−3.7520	−17.006	−33.770
		$\sigma_{zz}\,[10^6\,Pa]$ $(\tilde{z}/h = 0.75)$			
	12.920	2.8359	0.2196	0.0018	0.0002
		$\mathcal{D}_z\,[10^{-2}\,C/m^2]$ $(\tilde{z}/h = 1.00)$			
	−3.1042	−3.3419	−5.3519	−23.542	−46.878
		$g_z\,[10^{-5}\,kg/m^2]$ $(\tilde{z}/h = 1.00)$			
	−94.476	−90.646	−115.68	−455.32	−902.66

Results are obtained via the 3D-u-ϕ-$\mathcal{M}$ model. $\tilde{z}/h$ goes from 0 (bottom) to 1 (top).

Table 8 Benchmark B1, simply-supported multilayered rectangular plate in sensor closed circuit configuration ($\bar{P}_{z_t} = 10000\,Pa$, $\bar{P}_{z_b} = 0\,Pa$, $\bar{\Phi}_t = 0\,A$, $\bar{\Phi}_b = 0\,A$, $\bar{\mathcal{M}}_t = 1.5\,kg/m^3$, $\bar{\mathcal{M}}_b = 0.5\,kg/m^3$).

a/h	2	4	10	50	100
		$u\,[10^{-6}\,m]$ $(\tilde{z}/h = 0.00)$			
	−7.7426	−7.6316	−7.2892	−0.7106	19.745
		$w\,[10^{-5}\,m]$ $(\tilde{z}/h = 0.75)$			
	2.0571	3.0626	5.5974	46.007	222.04
		$\phi\,[A]$ $(\tilde{z}/h = 0.25)$			
	−114.94	−403.09	31.600	1363.88	2803.8
		$\mathcal{M}\,[kg/m^3]$ $(\tilde{z}/h = 0.25)$			
	0.2908	0.5463	0.7086	0.7483	0.7496
		$\sigma_{\alpha\beta}\,[10^6\,Pa]$ $(\tilde{z}/h = 0.75)$			
	−0.8749	−1.3684	−1.6549	−2.0172	−2.9479
		$\sigma_{zz}\,[10^4\,Pa]$ $(\tilde{z}/h = 0.75)$			
	−1.3883	0.4406	0.8270	0.8437	0.8437
		$\mathcal{D}_z\,[10^{-7}\,C/m^2]$ $(\tilde{z}/h = 1.00)$			
	4.5228	8.0001	9.3561	9.5555	9.5612
		$g_z\,[10^{-5}\,kg/m^2]$ $(\tilde{z}/h = 1.00)$			
	−94.476	−90.646	−115.68	−455.32	−902.66

Results are obtained via the 3D-u-ϕ-$\mathcal{M}$ model. $\tilde{z}/h$ goes from 0 (bottom) to 1 (top).

on Chebyshev polynomials combined with the Rayleigh–Ritz method, the finite element method, and the generalized finite element method. Rao *et al.* [23] employed the linear hygro−thermo−elastic theory for composites reinforced with multidirectional ellipsoidal fillers of arbitrary aspect ratio to predict the effective stiffness as well as the coefficients of thermal and moisture expansion of fiber-reinforced composites. A nonlinear hygro−thermo−mechanical formulation for curved thin and moderately thick shallow functionally graded panels was developed in [24]. Tocci Monaco *et al.* [25] investigated vibration and buckling phenomena in thin laminated composite nanoplates operating under hygrothermal conditions. Tornabene *et al.* [26] analyzed the stationary hygro−thermo−mechanical response of advanced laminated shell structures through an equivalent layer-wise two-dimensional formulation.

The consideration of hygrometric and thermal effects becomes even more relevant in smart structures incorporating piezoelectric and piezomagnetic layers. Arshid *et al.* [27] investigated the vibration characteristics of three-layered cylindrical shells subjected to

Downloaded from academic.oup.com/jom/article/doi/10.1093/jom/ufag025/8845483 by Politecnico di Torino user on 30 September 2026

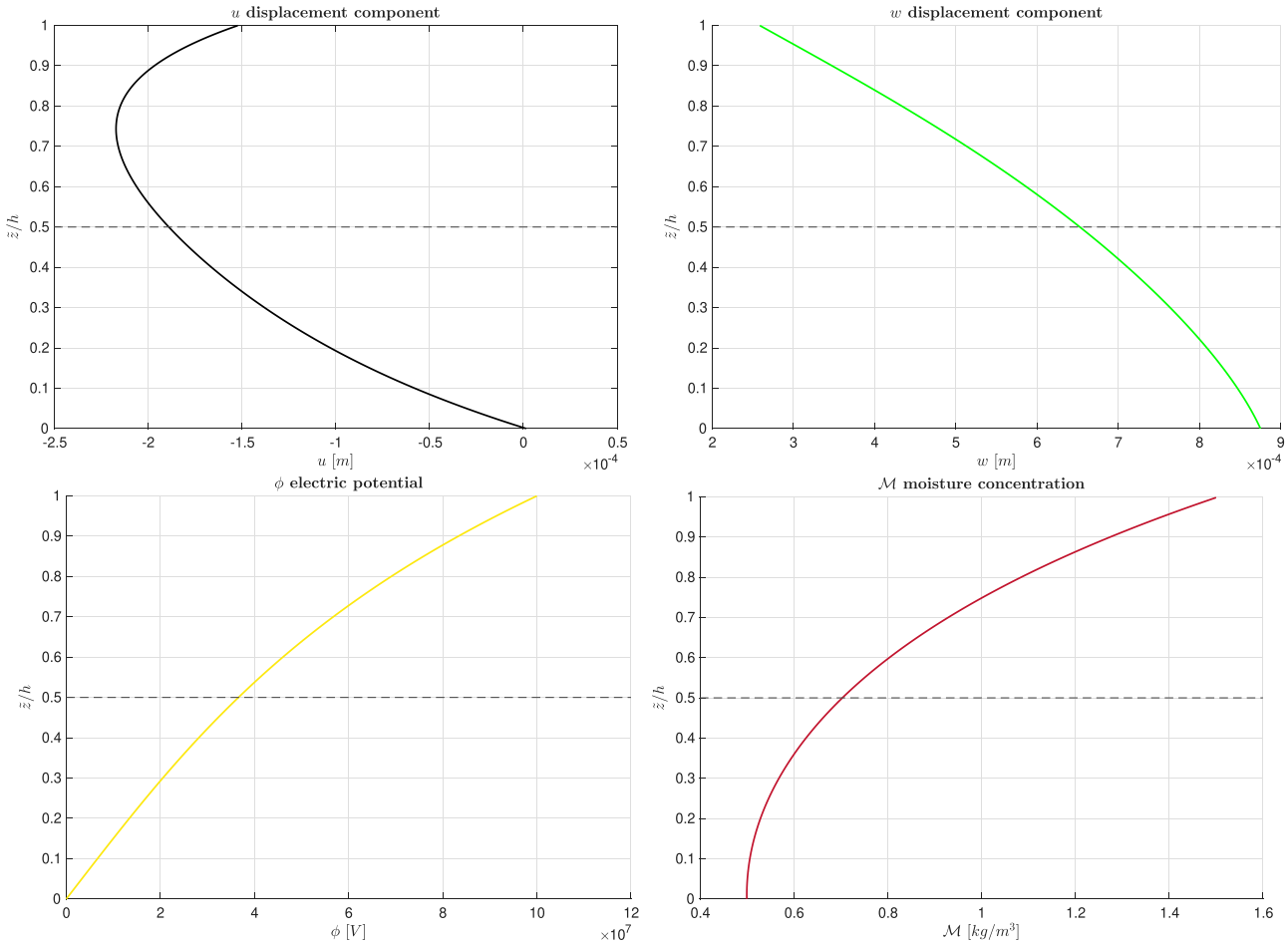

Figure 2 Benchmark B1, 3D-u-ϕ-$\mathcal{M}$ graphical trends along the thickness direction for the simply-supported multilayered plate in actuator configuration ($\bar{P}_{z_t} = 0\,Pa$, $\bar{P}_{z_b} = 0\,Pa$, $\bar{\Phi}_t = 1 \cdot 10^8\,A$, $\bar{\Phi}_b = 0\,A$, $\bar{\mathcal{M}}_t = 1.5\,kg/m^3$, $\bar{\mathcal{M}}_b = 0.5\,kg/m^3$) for $a/h = 4$.

hygro–magneto–electro–thermal loadings. Barati and Shariyat [28] derived an analytical solution for functionally graded magneto–electro–hygro–thermo–elastic discs exposed to different combinations of multifield actions. Dini and Abolbashari [29] carried out a theoretical investigation of thick-walled cylinders made of functionally graded piezoelectric materials under hygro–thermo–electro–mechanical loading conditions. In [30], a coupled nonlinear vibration formulation was introduced for composite cylindrical shells consisting of a carbon-nanotube-reinforced core and piezoelectric/piezomagnetic outer skins while accounting for hygro–thermo–electro–magnetic effects. Ebrahimi *et al.* [31] proposed a nonclassical beam formulation for the nonlinear vibration analysis of magneto–electro–hygro–thermal functionally graded piezoelectric nanobeams resting on an elastic foundation. Marzbanrad *et al.* [32] employed the nonlocal beam theory to study the hygro–electro–thermo–mechanical vibration response of functionally graded nanobeams subjected to magnetic fields and preload effects. In [33], the same authors developed a nonclassical formulation based on the extended piezoelectricity theory to investigate the nonlinear free vibration behavior of piezoelectric functionally graded nanobeams operating in hygro–magneto–electro–thermal environments. Nie *et al.* [34–36] introduced the stable node-based smoothed radial point interpolation method for three distinct applications: the dynamic analysis of hygro–thermo–magneto–electro–elastic coupled systems, the static analysis of hygro–thermo–electro–mechanical coupled problems involving functionally graded piezoelectric structures in hygrothermal environments, and the static and dynamic analyses of hygro–electro–mechanical multifield problems. Raja *et al.* [37] performed active stiffening and active compensation analyses to evaluate the effects of active stiffness on the dynamic response of piezo–hygro–thermo–elastic laminates. Tariq *et al.* [38] derived a general solution of the three-dimensional governing equations for transversely isotropic hygro–thermo–magneto–piezoelectric media using the potential theory approach. The same authors subsequently presented, in [39], a general solution for the plane problem of orthotropic hygro–electro–magneto–thermo–elastic materials. Tornabene *et al.* [40, 41] proposed an equivalent layer-wise two-dimensional multifield formulation for the analysis of laminated curved shells subjected to hygro–thermo–magneto–electro–elastic and hygro–thermo–electro–elastic couplings. Vinyas *et al.* [42] employed the finite element method to evaluate the coupled

Downloaded from academic.oup.com/jom/article/doi/10.1093/jom/ufag025/8845483 by Politecnico di Torino user on 30 September 2026

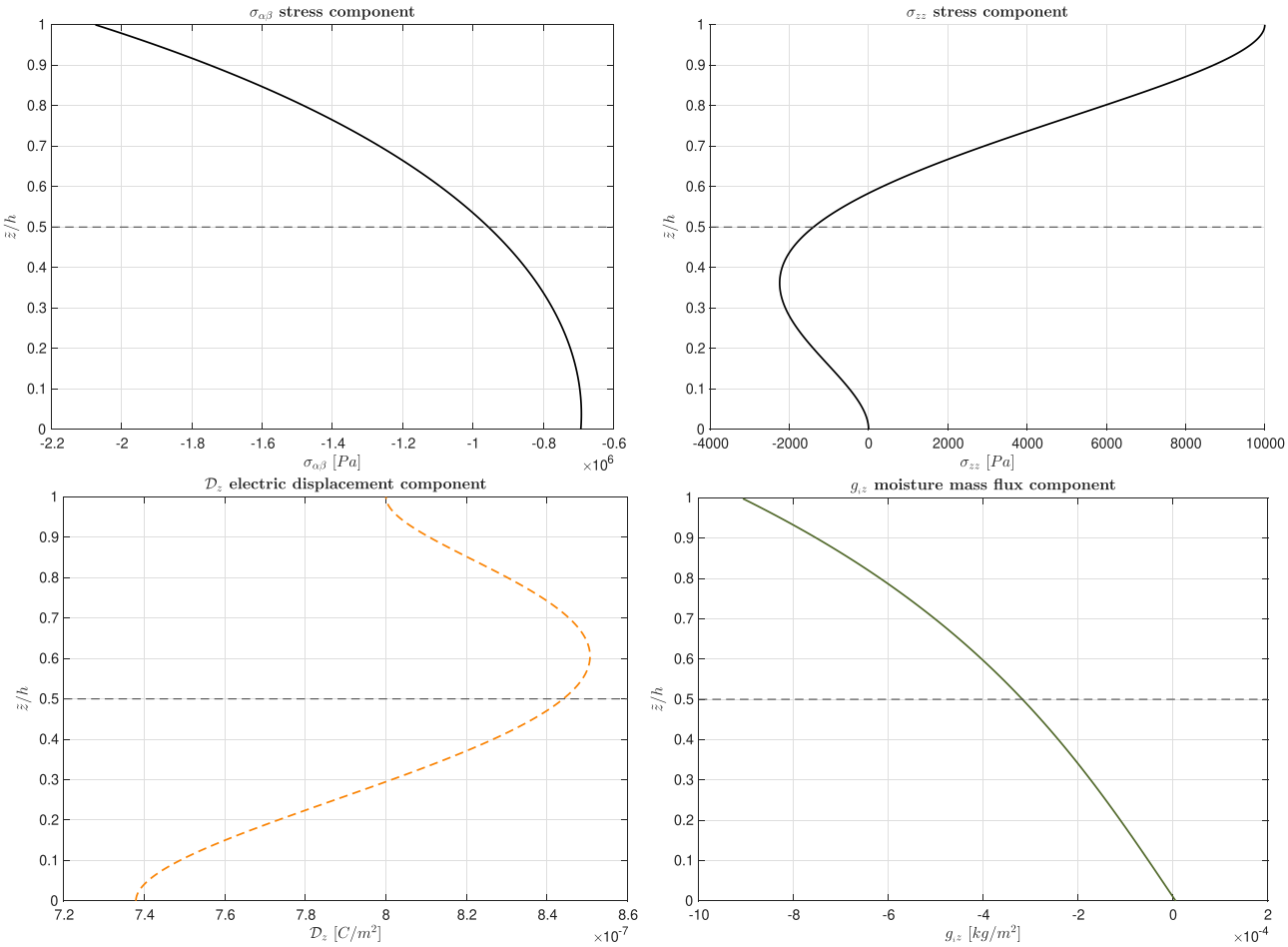

Figure 3 Benchmark B1, 3D-u-ϕ-$\mathcal{M}$ graphical trends along the thickness direction for the simply-supported multilayered plate in sensor closed circuit configuration ($\bar{P}_{z_t} = 10000\,Pa$, $\bar{P}_{z_b} = 0\,Pa$, $\bar{\Phi}_t = 0\,A$, $\bar{\Phi}_b = 0\,A$, $\bar{\mathcal{M}}_t = 1.5\,kg/m^3$, $\bar{\mathcal{M}}_b = 0.5\,kg/m^3$) for $a/h = 4$.

static response of hygro–thermo–magneto–electroelastic beams under hygrothermal loading conditions. Wang *et al.* [43] obtained an exact solution for the hygro–thermal–electro–elastic vibration problem of functionally graded piezoelectric composite cylindrical shells through a Hamiltonian-based framework. The multifield behavior of rotating functionally graded piezoelectric/piezomagnetic hollow cylinders subjected to magneto–electro–elasto–hygrothermal loadings was examined in [44]. Yang *et al.* [45] investigated buckling and post-buckling responses of simply supported microplates by considering elastic foundation effects together with hygro–thermal–electro–mechanical coupled loadings. Zenkour and Alghanmi [46] analyzed sandwich plates composed of a functionally graded core and piezoelectric face layers under sinusoidal hygrothermo–electro–mechanical excitations. In [47], an analytical solution was employed to investigate the interactions among electric potentials, electric displacement components, and elastic deformations in the hygrothermal response of inhomogeneous piezoelectric hollow cylinders. Zhang *et al.* [48, 49] presented isogeometric formulations for two coupled multiphysics scenarios, namely hygro–mechanical–electrical interactions in piezoelectric structures and hygro–thermo–electro–mechanical coupling in functionally graded piezoelectric systems. Zhou *et al.* [50] studied a piezoelectric beam subjected to multiphysical hygro–thermo–electro–mechanical couplings through the node-based smoothed radial point interpolation method.

From the literature survey discussed above, it emerges that only a limited number of studies have addressed shell structures involving the interaction of three or more physical fields, whereas most available contributions are devoted to beam and plate configurations. The availability of exact three-dimensional formulations is even more restricted. To contribute to this research area, the present work focuses on the coupling among hygrometric, electrical, and elastic fields and introduces an exact three-dimensional layer-wise formulation for the hygro–electro–elastic (HEE) analysis of multilayered shells. In addition, the simultaneous consideration of hygrometric, electrical, and mechanical fields is relevant to aerospace smart structures incorporating electrically active materials for sensing, actuation, or structural control, which may operate under combined mechanical and environmental loads. In such conditions, moisture diffusion can induce hygrometric strains and modify the local mechanical state, thereby affecting the response associated with the electrically active constituents. Furthermore, two-dimensional plate

Downloaded from academic.oup.com/jom/article/doi/10.1093/jom/ufag025/8845483 by Politecnico di Torino user on 30 September 2026

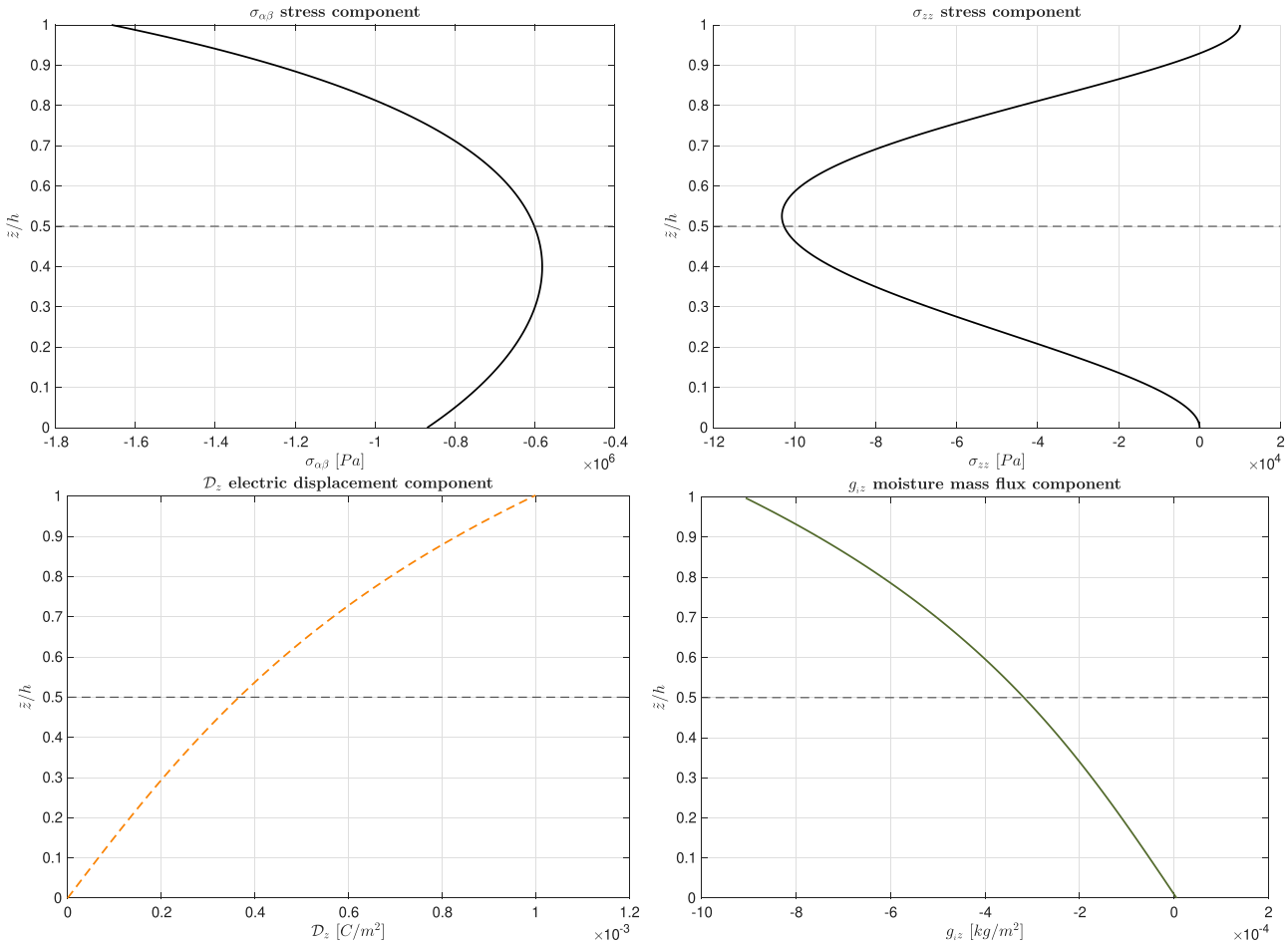

Figure 4 Benchmark B1, 3D-u-ϕ-$\mathcal{M}$ graphical trends along the thickness direction for the simply-supported multilayered plate in sensor open circuit configuration ($\bar{P}_{z_t} = 10000\,Pa$, $\bar{P}_{z_b} = 0\,Pa$, $\bar{\mathcal{D}}_{z_t} = 0.001\,C/m^2$, $\bar{\mathcal{D}}_{z_b} = 0\,C/m^2$, $\bar{\mathcal{M}}_t = 1.5\,kg/m^3$, $\bar{\mathcal{M}}_b = 0.5\,kg/m^3$) for $a/h = 4$.

or shell formulations generally cannot explicitly resolve the three-dimensional through-thickness distribution of moisture governed by Fick's diffusion equation, particularly in multilayered structures characterized by different material properties and layer thicknesses. The proposed three-dimensional formulation therefore enables the through-thickness distributions of moisture, electrical quantities, stresses, and displacements to be simultaneously resolved, providing information that is not directly accessible from conventional two-dimensional descriptions. The governing system for the static coupled HEE problem in spherical shells consists of five three-dimensional equations: three equilibrium equations, the divergence equation for the electric displacement field, and the Fick diffusion equation governing the moisture content. These equations are formulated within the orthogonal mixed curvilinear coordinate framework adopted for spherical shells. Through appropriate assumptions on the radii of curvature, the same formulation naturally reduces to the corresponding equations for plates, cylindrical panels, and cylinders. The coupling among the governing equations is achieved through suitable HEE geometrical and constitutive relationships. The resulting three-dimensional problem is solved by combining Navier harmonic expansions in the in-plane directions with the exponential matrix technique along the thickness coordinate. This solution procedure accurately captures the complete three-dimensional response through the thickness, providing displacement, electric potential, moisture content, stress, strain, moisture flux, and electric displacement distributions.

The remainder of the paper is structured as follows. The present section provides a literature review on the hygrometric field and its interactions with other physical fields in the context of multilayered aerospace structures. Section 2 describes the proposed three-dimensional HEE shell formulation together with the exponential matrix solution procedure implemented within a layer-wise framework. Section 3 contains both preliminary validation studies and newly generated results. The proposed formulation is assessed through comparisons with HEE models available in the literature. Furthermore, additional benchmark cases are presented by considering different thickness ratios, structural geometries (spherical shells, plates, cylindrical shells, and cylinders), and loading boundary conditions. Finally, Section 4 summarizes the main findings and concluding remarks of the study.

Downloaded from academic.oup.com/jom/article/doi/10.1093/jom/ufag025/8845483 by Politecnico di Torino user on 30 September 2026

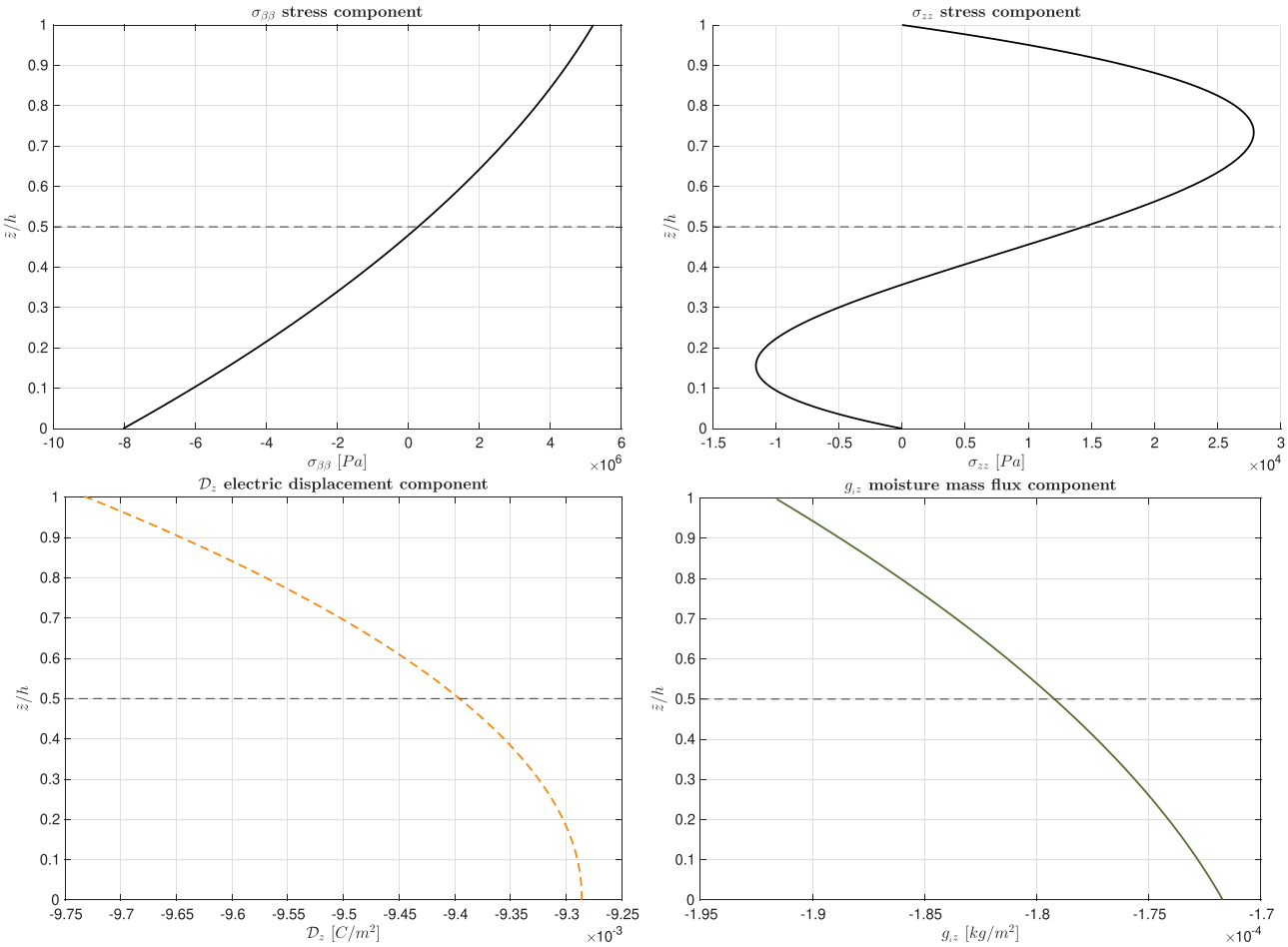

Figure 5 Benchmark B2, 3D-u-ϕ-$\mathcal{M}$ graphical trends along the thickness direction for the simply-supported multilayered cylinder in actuator configuration ($\bar{P}_{z_t} = 0\,Pa$, $\bar{P}_{z_b} = 0\,Pa$, $\bar{\Phi}_t = 1 \cdot 10^8\,A$, $\bar{\Phi}_b = 0\,A$, $\bar{\mathcal{M}}_t = 1.5\,kg/m^3$, $\bar{\mathcal{M}}_b = 0.5\,kg/m^3$) for $R_\alpha/h = 10$.

2. 3D multifield shell model

This section introduces the proposed three-dimensional static formulation for the coupled HEE analysis of spherical shells. The first subsection outlines the governing equations of the coupled problem within the mixed curvilinear orthogonal coordinate system (α, β, z). Figure 1 illustrates the adopted reference system together with the middle reference surface Ω_0 for the four structural configurations considered in this work. The second subsection presents the constitutive and geometrical relations governing the HEE behavior using the same coordinate framework. Finally, the solution strategy is described by detailing the combination of Navier harmonic expansions and the exponential matrix technique employed to obtain the strong-form solution of the three-dimensional governing equations.

2.1. 3D multifield governing equations

The static HEE problem for spherical shells is governed by five coupled three-dimensional equations. These relations consist of the three elastic equilibrium equations, the divergence equation associated with the electric displacement field, and the Fick diffusion equation governing moisture transport. All equations are formulated within the mixed curvilinear orthogonal coordinate system (α, β, z) adopted for spherical shell structures (see Fig. 1). The resulting set of governing equations is expressed as

$$H_\beta \sigma^k_{\alpha\alpha,\alpha} + H_\alpha \sigma^k_{\alpha\beta,\beta} + H_\alpha H_\beta \sigma^k_{\alpha z,z} + \left(\frac{2H_\beta}{R_\alpha} + \frac{H_\alpha}{R_\beta}\right)\sigma^k_{\alpha z} = 0, \quad (1)$$

$$H_\beta \sigma^k_{\alpha\beta,\alpha} + H_\alpha \sigma^k_{\beta\beta,\beta} + H_\alpha H_\beta \sigma^k_{\beta z,z} + \left(\frac{2H_\alpha}{R_\beta} + \frac{H_\beta}{R_\alpha}\right)\sigma^k_{\beta z} = 0, \quad (2)$$

$$H_\beta \sigma^k_{\alpha z,\alpha} + H_\alpha \sigma^k_{\beta z,\beta} + H_\alpha H_\beta \sigma^k_{zz,z} - \frac{H_\beta}{R_\alpha}\sigma^k_{\alpha\alpha} - \frac{H_\alpha}{R_\beta}\sigma^k_{\beta\beta} + \left(\frac{H_\beta}{R_\alpha} + \frac{H_\alpha}{R_\beta}\right)\sigma^k_{zz} = 0, \quad (3)$$

$$\frac{1}{H_\alpha}\mathcal{D}^k_{\alpha,\alpha} + \frac{1}{H_\beta}\mathcal{D}^k_{\beta,\beta} + \mathcal{D}^k_{z,z} = 0, \quad (4)$$

$$\frac{D^k_1}{H^2_\alpha}\mathcal{M}^k_{,\alpha\alpha} + \frac{D^k_2}{H^2_\beta}\mathcal{M}^k_{,\beta\beta} + D^k_3\mathcal{M}^k_{,zz} = 0. \quad (5)$$

In Eqs. (1)–(5), $\sigma^k_{\alpha\alpha}$, $\sigma^k_{\alpha\beta}$, $\sigma^k_{\alpha z}$, $\sigma^k_{\beta\beta}$, $\sigma^k_{\beta z}$, and σ^k_{zz} denote the six stress components. The quantities $\mathcal{D}^k_\alpha$, $\mathcal{D}^k_\beta$, and $\mathcal{D}^k_z$ represent the electric displacement components, whereas $\mathcal{M}^k$ identifies the scalar moisture content. The parameters D^k_1, D^k_2, and D^k_3 correspond to the moisture diffusion coefficients along the

Downloaded from academic.oup.com/jom/article/doi/10.1093/jom/ufag025/8845483 by Politecnico di Torino user on 30 September 2026

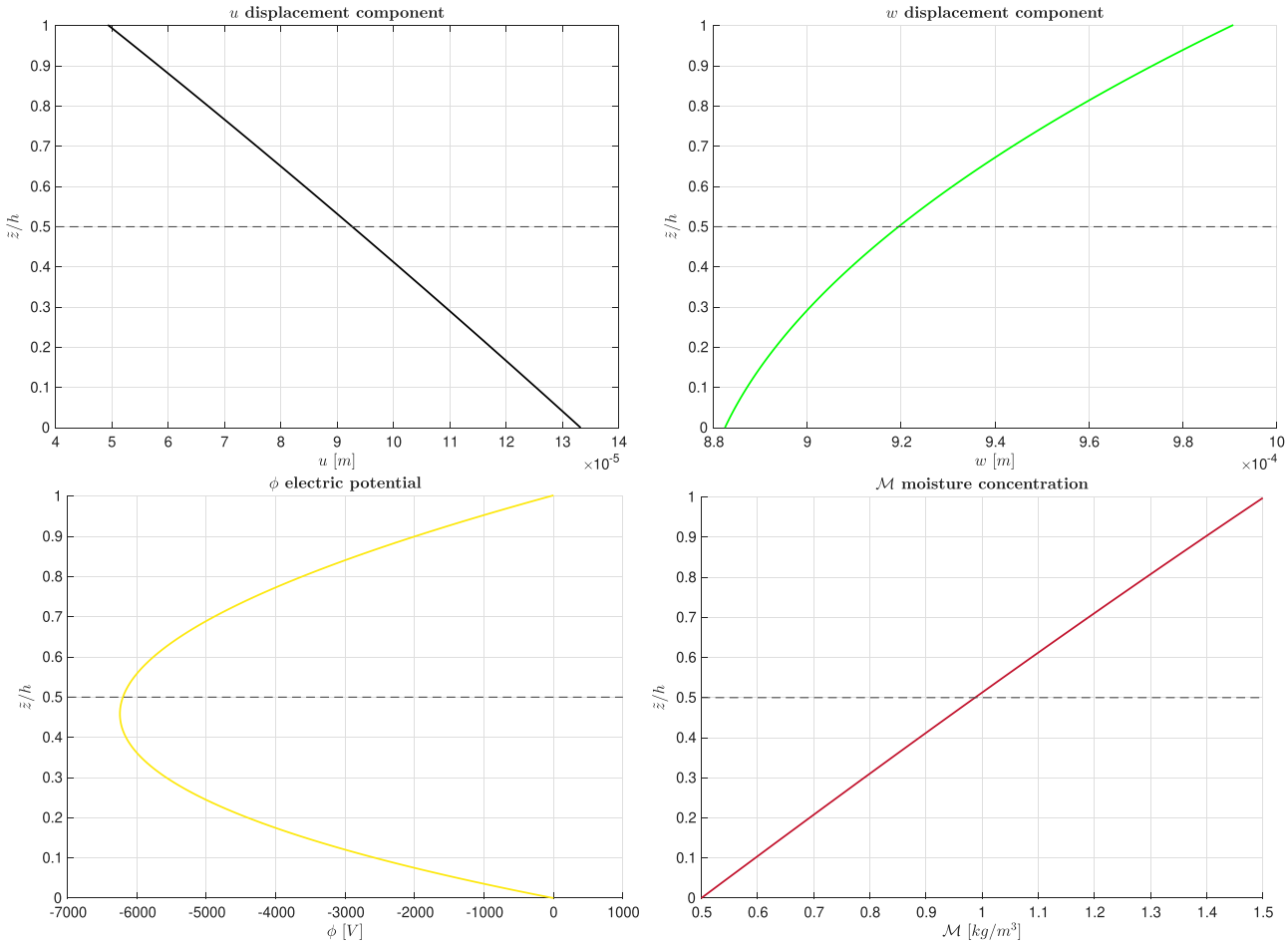

Figure 6 Benchmark B2, 3D-u-ϕ-$\mathcal{M}$ graphical trends along the thickness direction for the simply-supported multilayered cylinder in sensor closed circuit configuration ($\bar{P}_{z_t} = 10000\,Pa$, $\bar{P}_{z_b} = 0\,Pa$, $\bar{\Phi}_t = 0\,A$, $\bar{\Phi}_b = 0\,A$, $\bar{\mathcal{M}}_t = 1.5\,kg/m^3$, $\bar{\mathcal{M}}_b = 0.5\,kg/m^3$) for $R_\alpha/h = 10$.

three coordinate directions. The symbols $,\alpha$, $,\beta$, and $,z$ indicate partial differentiation with respect to the corresponding coordinates. The curvature parameters H_α and H_β depend on the shell geometry through the radii of curvature R_α and R_β evaluated on the middle reference surface Ω_0:

$$H_\alpha = \left(1 + \frac{z}{R_\alpha}\right) = \left(1 + \frac{\tilde{z} - h/2}{R_\alpha}\right),$$
$$H_\beta = \left(1 + \frac{z}{R_\beta}\right) = \left(1 + \frac{\tilde{z} - h/2}{R_\beta}\right), \quad H_z = 1. \tag{6}$$

The thickness coordinate z ranges from $-h/2$ to $h/2$, whereas the coordinate $\tilde{z}$ spans the interval $[0, h]$, with h denoting the total thickness of the structure. The origin of the z coordinate system is located at the upper-left corner of the middle surface Ω_0, while the origin associated with $\tilde{z}$ is positioned at the corresponding point on the bottom surface.

2.2. 3D multifield constitutive and geometrical equations

The constitutive relations governing the coupled HEE response are introduced to describe the orthotropic behavior of each lamina. The corresponding material properties establish the coupling among the elastic, electric, and hygrometric fields. For the generic kth layer, the constitutive equations are expressed as

$$\boldsymbol{\sigma}^k = \boldsymbol{C}^k \boldsymbol{\varepsilon}^k - \boldsymbol{e}^{kT} \boldsymbol{\mathcal{E}}^k - \boldsymbol{\xi}^k \mathcal{M}^k, \tag{7}$$
$$\boldsymbol{\mathcal{D}}^k = \boldsymbol{e}^k \boldsymbol{\varepsilon}^k + \boldsymbol{\epsilon}^k \boldsymbol{\mathcal{E}}^k - \boldsymbol{s}^k \mathcal{M}^k, \tag{8}$$
$$\boldsymbol{g}^k = -\boldsymbol{D}^k (\nabla \mathcal{M}^k), \tag{9}$$

where $\boldsymbol{\sigma}^k$ denotes the 6×1 stress vector (see Section 2.1), whereas $\boldsymbol{\mathcal{D}}^k$ represents the 3×1 electric displacement vector introduced in the same section. The scalar quantity $\mathcal{M}^k$ identifies the moisture content, whose value ranges between 0 and 1. The superscript T denotes the transpose operator. Throughout this work, each lamina is assumed to be orthotropic with a fiber orientation equal to 0° or 90° with respect to the structural reference system.

The elastic stiffness matrix is defined as

$$\boldsymbol{C}^k = \begin{bmatrix} C_{11}^k & C_{12}^k & C_{13}^k & 0 & 0 & 0 \\ C_{12}^k & C_{22}^k & C_{23}^k & 0 & 0 & 0 \\ C_{13}^k & C_{23}^k & C_{33}^k & 0 & 0 & 0 \\ 0 & 0 & 0 & C_{44}^k & 0 & 0 \\ 0 & 0 & 0 & 0 & C_{55}^k & 0 \\ 0 & 0 & 0 & 0 & 0 & C_{66}^k \end{bmatrix}. \tag{10}$$

Downloaded from academic.oup.com/jom/article/doi/10.1093/jom/ufag025/8845483 by Politecnico di Torino user on 30 September 2026

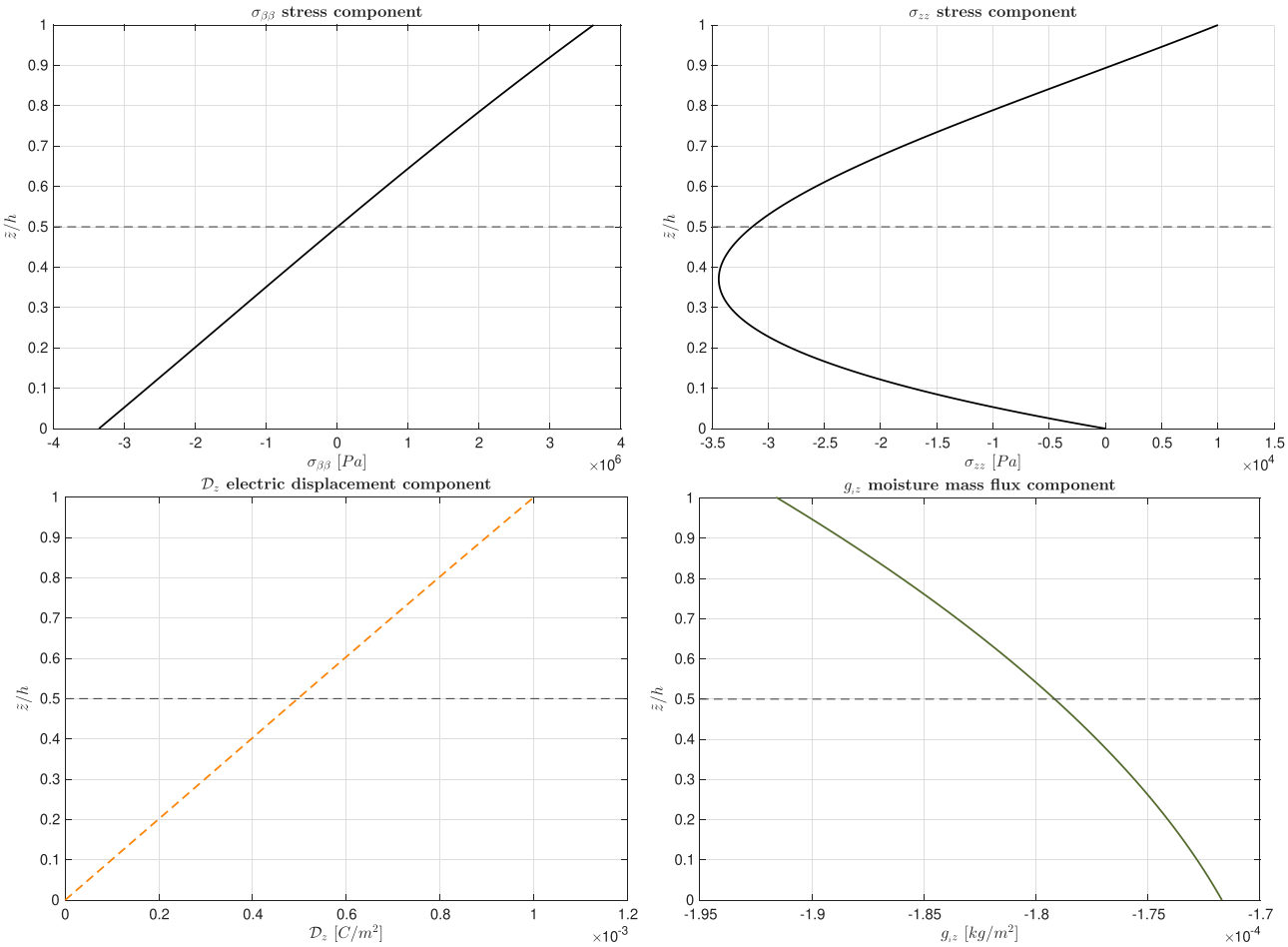

Figure 7 Benchmark B2, 3D-u-ϕ-$\mathcal{M}$ graphical trends along the thickness direction for the simply-supported multilayered cylinder in sensor open circuit configuration ($\bar{P}_{z_t} = 10000\,Pa$, $\bar{P}_{z_b} = 0\,Pa$, $\bar{\mathcal{D}}_{z_t} = 0.001\,C/m^2$, $\bar{\mathcal{D}}_{z_b} = 0\,C/m^2$, $\bar{\mathcal{M}}_t = 1.5\,kg/m^3$, $\bar{\mathcal{M}}_b = 0.5\,kg/m^3$) for $R_\alpha/h = 10$.

The associated strain vector reads

$$\boldsymbol{\varepsilon}^k = \begin{bmatrix} \varepsilon^k_{\alpha\alpha} \\ \varepsilon^k_{\beta\beta} \\ \varepsilon^k_{zz} \\ \gamma^k_{\beta z} \\ \gamma^k_{\alpha z} \\ \gamma^k_{\alpha\beta} \end{bmatrix}. \tag{11}$$

The piezoelectric coupling matrix is given by

$$\boldsymbol{e}^k = \begin{bmatrix} 0 & 0 & 0 & 0 & e^k_{15} & 0 \\ 0 & 0 & 0 & e^k_{24} & 0 & 0 \\ e^k_{31} & e^k_{32} & e^k_{33} & 0 & 0 & 0 \end{bmatrix}. \tag{12}$$

The electric field vector takes the form

$$\boldsymbol{\mathcal{E}}^k = \begin{bmatrix} \mathcal{E}^k_\alpha \\ \mathcal{E}^k_\beta \\ \mathcal{E}^k_z \end{bmatrix}. \tag{13}$$

The hygro−elastic coupling vector is obtained as the product of the elastic stiffness matrix $\boldsymbol{C}^k$ and the hygrometric expansion coefficient vector $\boldsymbol{\eta}^k$:

$$\boldsymbol{\xi}^k = \begin{Bmatrix} \xi^k_{11} \\ \xi^k_{22} \\ \xi^k_{33} \\ 0 \\ 0 \\ 0 \end{Bmatrix} = \boldsymbol{C}^k \boldsymbol{\eta}^k = \boldsymbol{C}^k \begin{Bmatrix} \eta^k_{11} \\ \eta^k_{22} \\ \eta^k_{33} \\ 0 \\ 0 \\ 0 \end{Bmatrix}. \tag{14}$$

The electric permittivity matrix is

$$\boldsymbol{\epsilon}^k = \begin{bmatrix} \epsilon^k_{11} & 0 & 0 \\ 0 & \epsilon^k_{22} & 0 \\ 0 & 0 & \epsilon^k_{33} \end{bmatrix}. \tag{15}$$

The hygro−electric coupling vector is defined as

$$\boldsymbol{s}^k = \begin{Bmatrix} 0 \\ 0 \\ s^k_3 \end{Bmatrix}. \tag{16}$$

The moisture flux vector is expressed by

$$\boldsymbol{g}^k = \begin{Bmatrix} g^k_\alpha \\ g^k_\beta \\ g^k_z \end{Bmatrix}. \tag{17}$$

Downloaded from academic.oup.com/jom/article/doi/10.1093/jom/ufag025/8845483 by Politecnico di Torino user on 30 September 2026

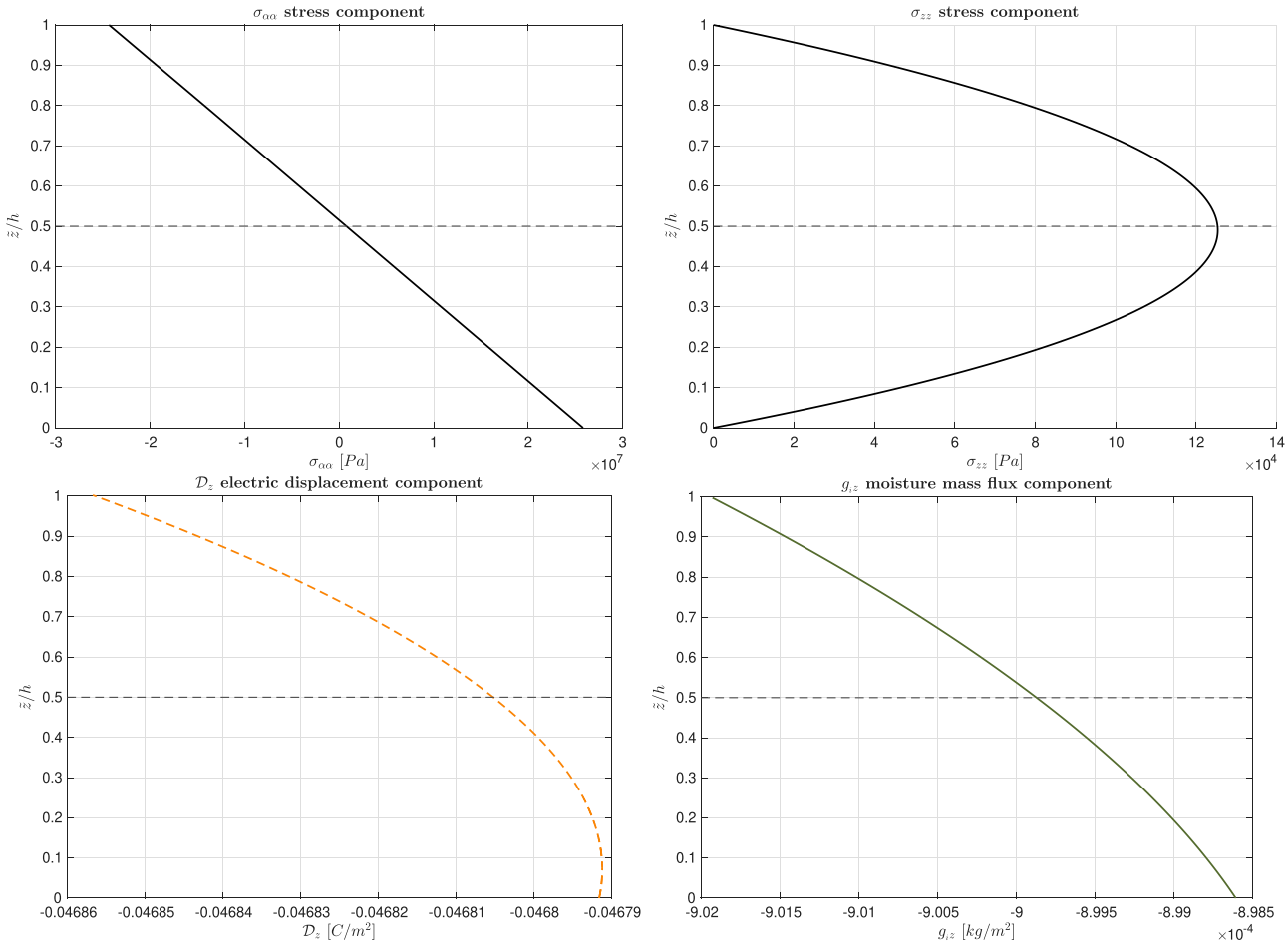

Figure 8 Benchmark B3, 3D-u-ϕ-$\mathcal{M}$ graphical trends along the thickness direction for the simply-supported multilayered cylindrical panel in actuator configuration ($\bar{P}_{z_t} = 0\,Pa$, $\bar{P}_{z_b} = 0\,Pa$, $\bar{\Phi}_t = 1 \cdot 10^8\,A$, $\bar{\Phi}_b = 0\,A$, $\bar{\mathcal{M}}_t = 1.5\,kg/m^3$, $\bar{\mathcal{M}}_b = 0.5\,kg/m^3$) for $R_\alpha/h = 50$.

The moisture diffusion coefficients are collected into the diagonal matrix

$$\boldsymbol{D}^k = \begin{bmatrix} D^k_{11} & 0 & 0 \\ 0 & D^k_{22} & 0 \\ 0 & 0 & D^k_{33} \end{bmatrix}. \tag{18}$$

Finally, the gradient operator associated with the mixed curvilinear orthogonal coordinate system is written as

$$\nabla = \begin{bmatrix} \frac{1}{H_\alpha}\frac{\partial}{\partial\alpha} \\ \frac{1}{H_\beta}\frac{\partial}{\partial\beta} \\ \frac{\partial}{\partial z} \end{bmatrix}. \tag{19}$$

The geometrical relations establish the kinematic connection between the strain field and the displacement components, whereas the electric field is obtained from the gradient of the electric potential according to

$$\boldsymbol{\varepsilon}^k = \boldsymbol{\Delta}\,\boldsymbol{u}^k, \tag{20}$$

$$\boldsymbol{\mathcal{E}}^k = -\nabla\,\phi^k, \tag{21}$$

where ϕ^k denotes the scalar electric potential and $\boldsymbol{\Delta}$ is the 6×3 differential operator associated with the elastic field for spherical shell geometries:

$$\boldsymbol{\Delta} = \begin{bmatrix} \frac{1}{H_\alpha}\frac{\partial}{\partial\alpha} & 0 & \frac{1}{H_\alpha R_\alpha} \\ 0 & \frac{1}{H_\beta}\frac{\partial}{\partial\beta} & \frac{1}{H_\beta R_\beta} \\ 0 & 0 & \frac{\partial}{\partial z} \\ 0 & \frac{\partial}{\partial z} - \frac{1}{H_\beta R_\beta} & \frac{1}{H_\beta}\frac{\partial}{\partial\beta} \\ \frac{\partial}{\partial z} - \frac{1}{H_\alpha R_\alpha} & 0 & \frac{1}{H_\alpha}\frac{\partial}{\partial\alpha} \\ \frac{1}{H_\beta}\frac{\partial}{\partial\beta} & \frac{1}{H_\alpha}\frac{\partial}{\partial\alpha} & 0 \end{bmatrix}. \tag{22}$$

The displacement field is represented by the vector

$$\boldsymbol{u}^k = \begin{bmatrix} u^k \\ v^k \\ w^k \end{bmatrix}. \tag{23}$$

2.3. Strong-form solution procedure

The solution strategy is based on the adoption of Navier harmonic expansions in the in-plane coordinates α and β. Accordingly, the displacement components, the electric potential, and the moisture content are approximated through the following harmonic representations:

$$u(\alpha,\beta,z)^k = U^k(z)\cos(\bar{\alpha}\alpha)\sin(\bar{\beta}\beta), \tag{24}$$

$$v(\alpha,\beta,z)^k = V^k(z)\sin(\bar{\alpha}\alpha)\cos(\bar{\beta}\beta), \tag{25}$$

Downloaded from academic.oup.com/jom/article/doi/10.1093/jom/ufag025/8845483 by Politecnico di Torino user on 30 September 2026

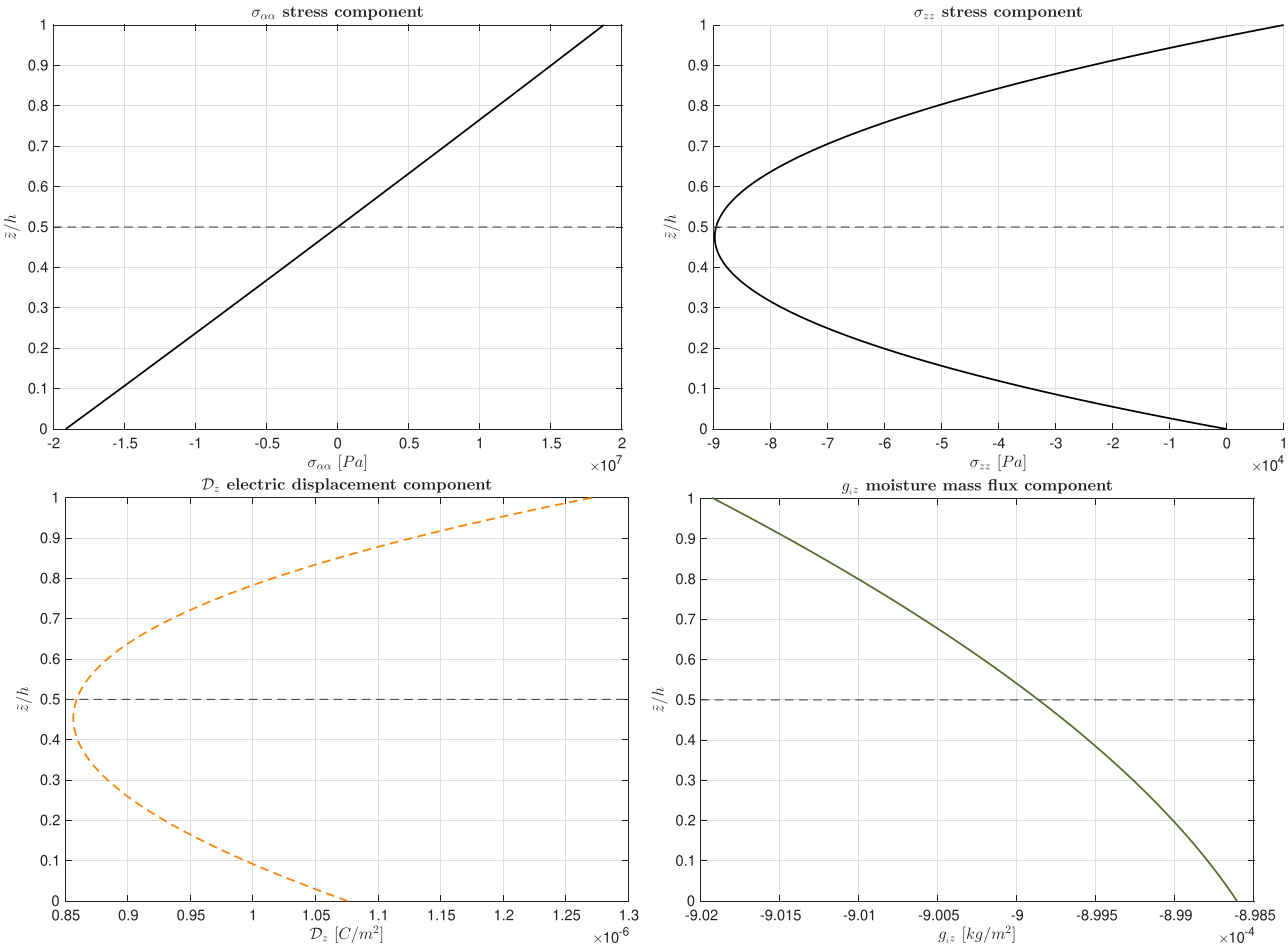

Figure 9 Benchmark B3, 3D-u-ϕ-$\mathcal{M}$ graphical trends along the thickness direction for the simply-supported multilayered cylindrical panel in sensor closed circuit configuration ($\bar{P}_{z_t} = 10000\,Pa$, $\bar{P}_{z_b} = 0\,Pa$, $\bar{\Phi}_t = 0\,A$, $\bar{\Phi}_b = 0\,A$, $\bar{\mathcal{M}}_t = 1.5\,kg/m^3$, $\bar{\mathcal{M}}_b = 0.5\,kg/m^3$) for $R_\alpha/h = 50$.

$$(w(\alpha,\beta,z)^k, \phi(\alpha,\beta,z)^k, \mathcal{M}(\alpha,\beta,z)^k) = (W^k(z), \Phi^k(z), M^k(z)) \sin(\bar{\alpha}\alpha)\sin(\bar{\beta}\beta). \tag{26}$$

The $\bar{\alpha}$ and $\bar{\beta}$ scale factor for sine and cosine trigonometric functions are defined as follows:

$$\bar{\alpha} = \frac{m\pi}{a}, \qquad \bar{\beta} = \frac{n\pi}{b} \tag{27}$$

where m and n are the half-wave number in the α and β directions and a and b are the in-plane dimensions of the geometry.

Since the harmonic expansions defined in Eqs. (24)–(26) are adopted over the in-plane domain, the corresponding admissible boundary conditions are restricted to simply-supported edges. These conditions can be written as:

$$\begin{aligned} &v^k = 0, \quad w^k = 0, \quad \phi^k = 0, \quad \mathcal{M}^k = 0, \quad \sigma^k_{\alpha\alpha} = 0 \\ &\qquad \text{for} \quad \alpha = 0, a, \\ &u^k = 0, \quad w^k = 0, \quad \phi^k = 0, \quad \mathcal{M}^k = 0, \quad \sigma^k_{\beta\beta} = 0 \\ &\qquad \text{for} \quad \beta = 0, b. \end{aligned} \tag{28}$$

Substituting the harmonic expansions given by Eqs. (24)–(26) into the governing equations (1)–(5), together with the constitutive relations (7)–(9) and the kinematic relations (20)–(21), transforms the original system of coupled partial differential equations into a system of ordinary differential equations with respect to the thickness coordinate z. The unknown amplitudes are the displacement functions $U^k(z)$, $V^k(z)$, and $W^k(z)$, together with the electric potential amplitude $\Phi^k(z)$ and the moisture content amplitude $M^k(z)$, which constitute the primary variables of the coupled HEE problem. The resulting governing equations can therefore be written as

$$\begin{aligned} &\left(-\frac{H_\beta C^k_{55}}{H_\alpha R^2_\alpha} - \frac{C^k_{55}}{R_\alpha R_\beta} - \bar{\alpha}^2 \frac{C^k_{11} H_\beta}{H_\alpha} - \bar{\beta}^2 \frac{C^k_{66} H_\alpha}{H_\beta}\right) U^k \\ &+ \left(-\bar{\alpha}\bar{\beta} C^k_{12} - \bar{\alpha}\bar{\beta} C^k_{66}\right) V^k + \left(\bar{\alpha}\frac{C^k_{11} H_\beta}{H_\alpha R_\alpha} + \bar{\alpha}\frac{C^k_{12}}{R_\beta} + \bar{\alpha}\frac{C^k_{55} H_\beta}{H_\alpha R_\alpha} + \bar{\alpha}\frac{C^k_{55}}{R_\beta}\right) W^k \\ &+ \left(\frac{C^k_{55} H_\beta}{R_\alpha} + \frac{C^k_{55} H_\alpha}{R_\beta}\right) U^k_{,z} + \left(\bar{\alpha} C^k_{13} H_\beta + \bar{\alpha} C^k_{55} H_\beta\right) W^k_{,z} \\ &+ \left(C^k_{55} H_\alpha H_\beta\right) U^k_{,zz} + \left(2\bar{\alpha}\frac{e^k_{15} H_\beta}{H_\alpha R_\alpha} + \bar{\alpha}\frac{e^k_{15}}{R_\beta}\right) \Phi^k \\ &+ \left(\bar{\alpha} e^k_{31} H_\beta + \bar{\alpha} e^k_{15} H_\beta\right) \Phi^k_{,z} + \left(-\bar{\alpha}\xi^k_{11} H_\beta\right) M^k = 0, \end{aligned} \tag{29}$$

Downloaded from academic.oup.com/jom/article/doi/10.1093/jom/ufag025/8845483 by Politecnico di Torino user on 30 September 2026

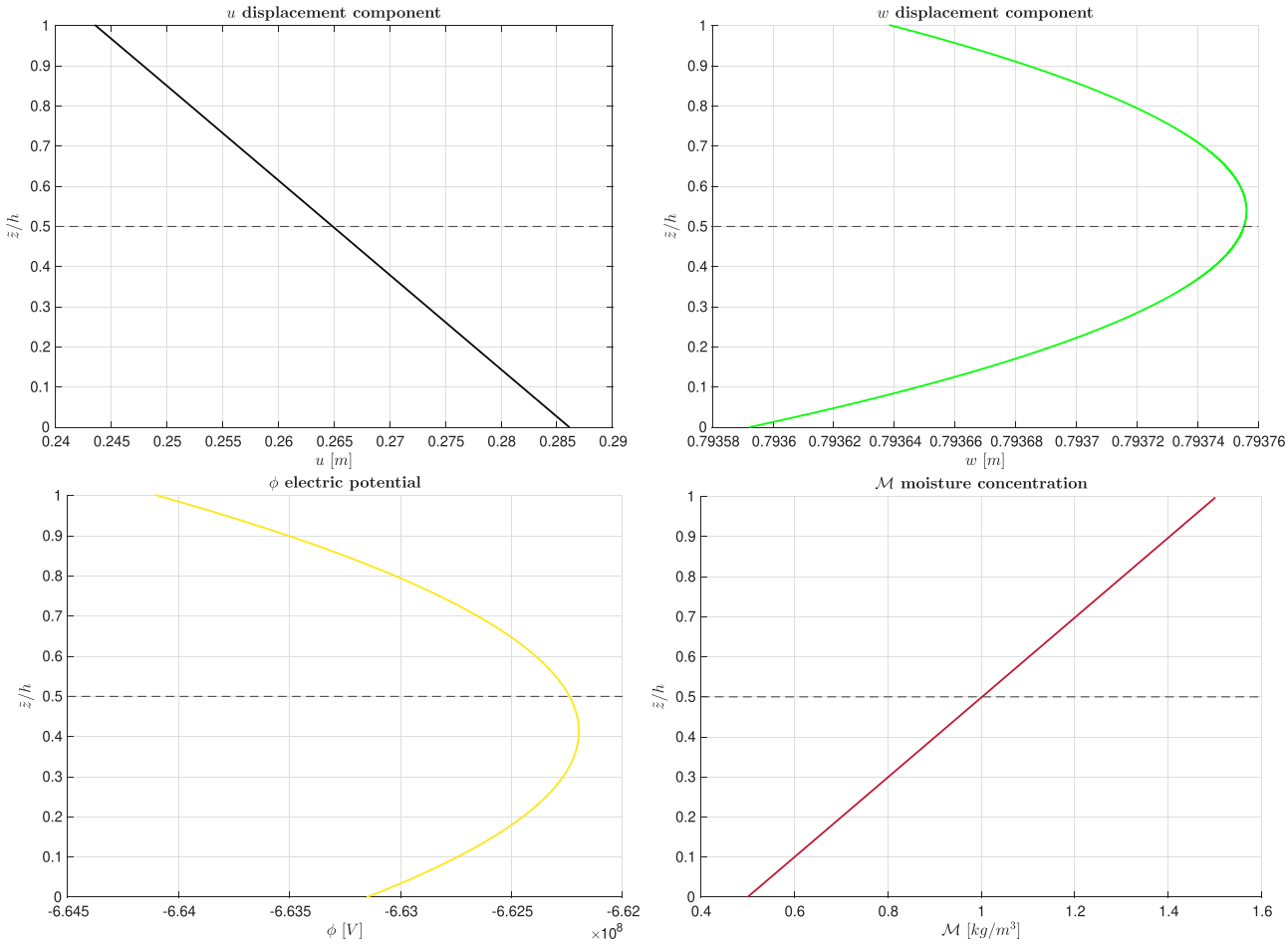

Figure 10 Benchmark B3, 3D-u-ϕ-$\mathcal{M}$ graphical trends along the thickness direction for the simply-supported multilayered cylindrical panel in sensor open circuit configuration ($\bar{P}_{z_t} = 10000\,Pa$, $\bar{P}_{z_b} = 0\,Pa$, $\bar{\mathcal{D}}_{z_t} = 0.001\,C/m^2$, $\bar{\mathcal{D}}_{z_b} = 0\,C/m^2$, $\bar{\mathcal{M}}_t = 1.5\,kg/m^3$, $\bar{\mathcal{M}}_b = 0.5\,kg/m^3$) for $R_\alpha/h = 50$.

$$
\begin{aligned}
&\left(-\frac{H_\alpha C_{44}^k}{H_\beta R_\beta^2} - \frac{C_{44}^k}{R_\alpha R_\beta} - \bar{\alpha}^2\frac{C_{66}^k H_\beta}{H_\alpha} - \bar{\beta}^2\frac{C_{22}^k H_\alpha}{H_\beta}\right) V^k \\
&+ \left(-\bar{\alpha}\bar{\beta}C_{12}^k - \bar{\alpha}\bar{\beta}C_{66}^k\right) U^k \\
&+ \left(\bar{\beta}\frac{C_{44}^k H_\alpha}{H_\beta R_\beta} + \bar{\beta}\frac{C_{44}^k}{R_\alpha} + \bar{\beta}\frac{C_{22}^k H_\alpha}{H_\beta R_\beta} + \bar{\beta}\frac{C_{12}^k}{R_\alpha}\right) W^k \\
&+ \left(\frac{C_{44}^k H_\alpha}{R_\beta} + \frac{C_{44}^k H_\beta}{R_\alpha}\right) V_{,z}^k \\
&+ \left(\bar{\beta}C_{44}^k H_\alpha + \bar{\beta}C_{23}^k H_\alpha\right) W_{,z}^k + \left(C_{44}^k H_\alpha H_\beta\right) V_{,zz}^k \\
&+ \left(2\bar{\beta}\frac{e_{24}^k H_\alpha}{H_\beta R_\beta} + \bar{\beta}\frac{e_{24}^k}{R_\alpha}\right) \Phi^k \\
&+ \left(\bar{\beta}e_{32}^k H_\alpha + \bar{\beta}e_{24}^k H_\alpha\right) \Phi_{,z}^k + \left(-\bar{\beta}\xi_{22}^k H_\alpha\right) M^k = 0, \quad (30)
\end{aligned}
$$

$$
\begin{aligned}
&\left(\frac{C_{13}^k}{R_\alpha R_\beta} + \frac{C_{23}^k}{R_\alpha R_\beta} - \frac{C_{11}^k H_\beta}{H_\alpha R_\alpha^2} - \frac{2C_{12}^k}{R_\alpha R_\beta} - \frac{C_{22}^k H_\alpha}{H_\beta R_\beta^2} - \bar{\alpha}^2\frac{C_{55}^k H_\beta}{H_\alpha} - \bar{\beta}^2\frac{C_{44}^k H_\alpha}{H_\beta}\right) W^k \\
&+ \left(\bar{\alpha}\frac{C_{55}^k H_\beta}{H_\alpha R_\alpha} - \bar{\alpha}\frac{C_{13}^k}{R_\beta} + \bar{\alpha}\frac{C_{11}^k H_\beta}{H_\alpha R_\alpha} + \bar{\alpha}\frac{C_{12}^k}{R_\beta}\right) U^k \\
&+ \left(\bar{\beta}\frac{C_{44}^k H_\alpha}{H_\beta R_\beta} - \bar{\beta}\frac{C_{23}^k}{R_\alpha} + \bar{\beta}\frac{C_{22}^k H_\alpha}{H_\beta R_\beta} + \bar{\beta}\frac{C_{12}^k}{R_\alpha}\right) V^k \\
&+ \left(-\bar{\alpha}C_{55}^k H_\beta - \bar{\alpha}C_{13}^k H_\beta\right) U_{,z}^k + \left(-\bar{\beta}C_{44}^k H_\alpha - \bar{\beta}C_{23}^k H_\alpha\right) V_{,z}^k \\
&+ \left(\frac{C_{33}^k H_\beta}{R_\alpha} + \frac{C_{33}^k H_\alpha}{R_\beta}\right) W_{,z}^k \\
&+ \left(C_{33}^k H_\alpha H_\beta\right) W_{,zz}^k + \left(-\bar{\alpha}^2\frac{e_{15}^k H_\beta}{H_\alpha} - \bar{\beta}^2\frac{e_{24}^k H_\alpha}{H_\beta}\right) \Phi^k \\
&+ \left(-\frac{e_{31}^k H_\beta}{R_\alpha} - \frac{e_{32}^k H_\alpha}{R_\beta} + \frac{e_{33}^k H_\beta}{R_\alpha} + \frac{e_{33}^k H_\alpha}{R_\beta}\right) \Phi_{,z}^k \\
&\left(e_{33}^k H_\alpha H_\beta\right) \Phi_{,zz}^k + \left(\frac{\xi_{11}^k H_\beta}{R_\alpha} + \frac{\xi_{22}^k H_\alpha}{R_\beta} - \frac{\xi_{33}^k H_\beta}{R_\alpha} - \frac{\xi_{33}^k H_\alpha}{R_\beta}\right) M^k \\
&+ \left(-\xi_{33}^k H_\alpha H_\beta\right) M_{,z}^k = 0, \quad (31)
\end{aligned}
$$

Downloaded from academic.oup.com/jom/article/doi/10.1093/jom/ufag025/8845483 by Politecnico di Torino user on 30 September 2026

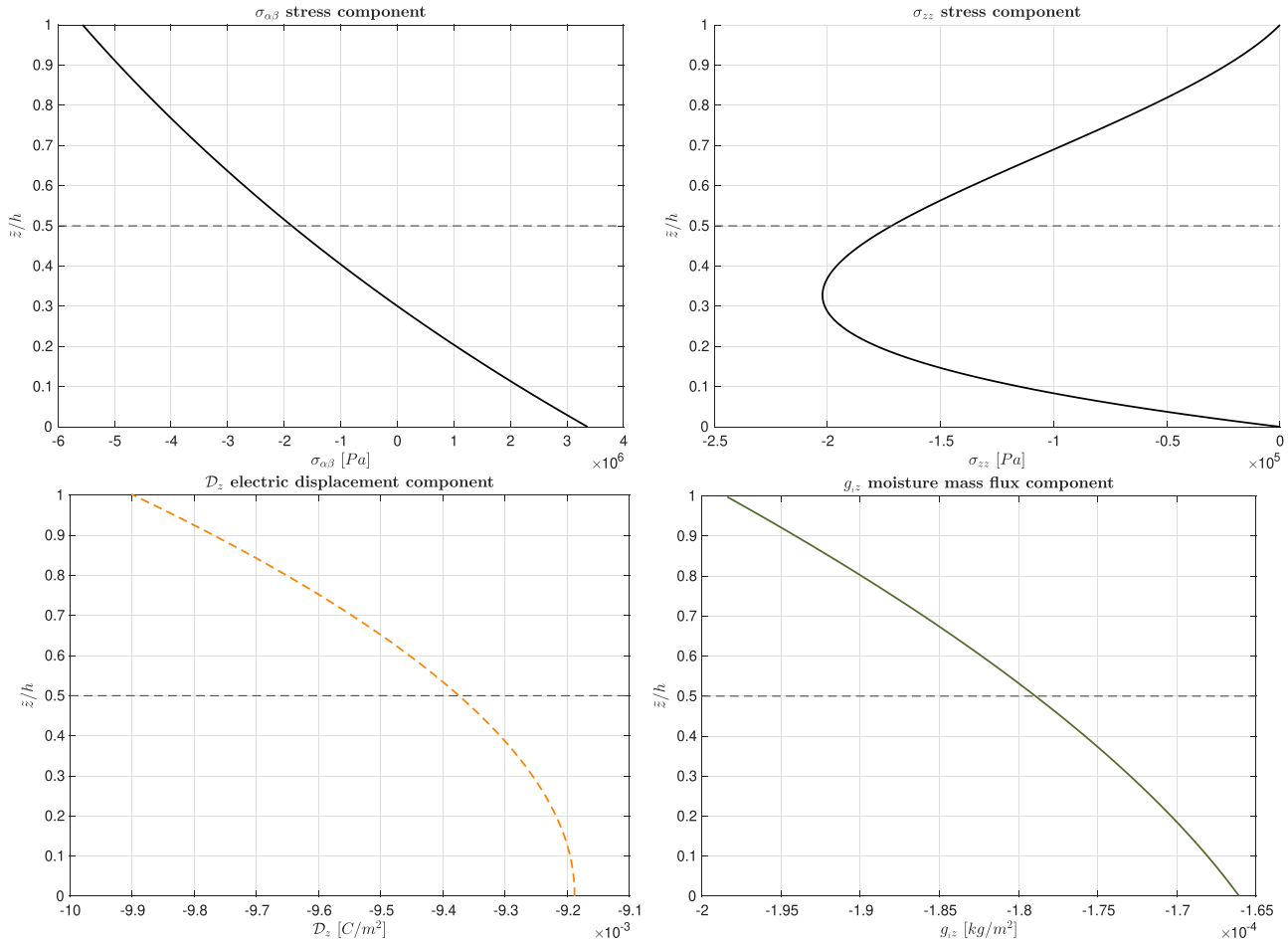

Figure 11 Benchmark B4, 3D-u-ϕ-$\mathcal{M}$ graphical trends along the thickness direction for the simply-supported multilayered spherical shell in actuator configuration ($\bar{P}_{z_t} = 0\,Pa$, $\bar{P}_{z_b} = 0\,Pa$, $\bar{\Phi}_t = 1 \cdot 10^8\,A$, $\bar{\Phi}_b = 0\,A$, $\bar{\mathcal{M}}_t = 1.5\,kg/m^3$, $\bar{\mathcal{M}}_b = 0.5\,kg/m^3$) for $R_\alpha/h = 10$.

$$\left(\bar{\alpha}\frac{e_{15}^k}{H_\alpha^2 R_\alpha}\right)U^k + \left(\bar{\beta}\frac{e_{24}^k}{H_\beta^2 R_\beta}\right)V^k + \left(-\bar{\alpha}^2\frac{e_{15}^k}{H_\alpha^2} - \bar{\beta}^2\frac{e_{24}^k}{H_\beta^2}\right)W^k + \left(-\bar{\alpha}\frac{e_{15}^k}{H_\alpha} - \bar{\alpha}\frac{e_{31}^k}{H_\alpha}\right)U_{,z}^k + \left(-\bar{\beta}\frac{e_{24}^k}{H_\beta} - \bar{\beta}\frac{e_{32}^k}{H_\beta}\right)V_{,z}^k + \left(\frac{e_{31}^k}{H_\alpha R_\alpha} + \frac{e_{32}^k}{H_\beta R_\beta}\right)W_{,z}^k + \left(e_{33}^k\right)W_{,zz}^k + \left(\bar{\alpha}^2\frac{\epsilon_{11}^k}{H_\alpha^2} + \bar{\beta}^2\frac{\epsilon_{22}^k}{H_\beta^2}\right)\Phi^k - \left(\epsilon_{33}^k\right)\Phi_{,zz}^k + \left(s_3^k\right)M_{,z}^k = 0, \quad (32)$$

$$\left(-\bar{\alpha}^2\frac{D_{11}^k}{H_\alpha^2} - \bar{\beta}^2\frac{D_{22}^k}{H_\beta^2}\right)M^k + \left(D_{33}^k\right)M_{,zz}^k = 0. \quad (33)$$

To simplify the notation, all the coefficients appearing in parentheses in Eqs. (29)–(33) are collected into auxiliary coefficients. Consequently, the governing equations assume the following compact form:

$$A_1^k U^k + A_2^k V^k + A_3^k W^k + A_4^k \Phi^k + J_1^k M^k + A_5^k U_{,z}^k + A_6^k W_{,z}^k + A_7^k \Phi_{,z}^k + A_8^k U_{,zz}^k = 0, \quad (34)$$

$$A_9^k U^k + A_{10}^k V^k + A_{11}^k W^k + A_{12}^k \Phi^k + J_2^k M^k + A_{13}^k V_{,z}^k + A_{14}^k W_{,z}^k + A_{15}^k \Phi_{,z}^k + A_{16}^k V_{,zz}^k = 0, \quad (35)$$

$$A_{17}^k U^k + A_{18}^k V^k + A_{19}^k W^k + A_{20}^k \Phi^k + J_3^k M^k + A_{21}^k U_{,z}^k + A_{22}^k V_{,z}^k + A_{23}^k W_{,z}^k + A_{24}^k \Phi_{,z}^k + J_4^k M_{,z}^k + A_{25}^k W_{,zz}^k + A_{26}^k \Phi_{,zz}^k = 0, \quad (36)$$

$$A_{27}^k U^k + A_{28}^k V^k + A_{29}^k W^k + A_{30}^k \Phi^k + A_{31}^k U_{,z}^k + A_{32}^k V_{,z}^k + A_{33}^k W_{,z}^k + J_5^k M_{,z}^k + A_{34}^k W_{,zz}^k + A_{35}^k \Phi_{,zz}^k = 0, \quad (37)$$

$$J_6^k M^k + J_7^k M_{,zz}^k = 0. \quad (38)$$

The compact system of second-order ordinary differential equations with respect to the thickness coordinate z must now be transformed into a form suitable for the application of the exponential matrix technique. This procedure requires a first-order differential system with constant coefficients. To satisfy the latter requirement, each physical layer is subdivided into a suitable number of mathematical sublayers, so that the curvature parameters H_α and H_β can be assumed constant within each sublayer. Consequently, all the coefficients A_i^k and J_i^k also become constant. The order reduction is then performed by introducing the first derivatives of the primary variables as additional unknowns. Accordingly, the state variables of

Downloaded from academic.oup.com/jom/article/doi/10.1093/jom/ufag025/8845483 by Politecnico di Torino user on 30 September 2026

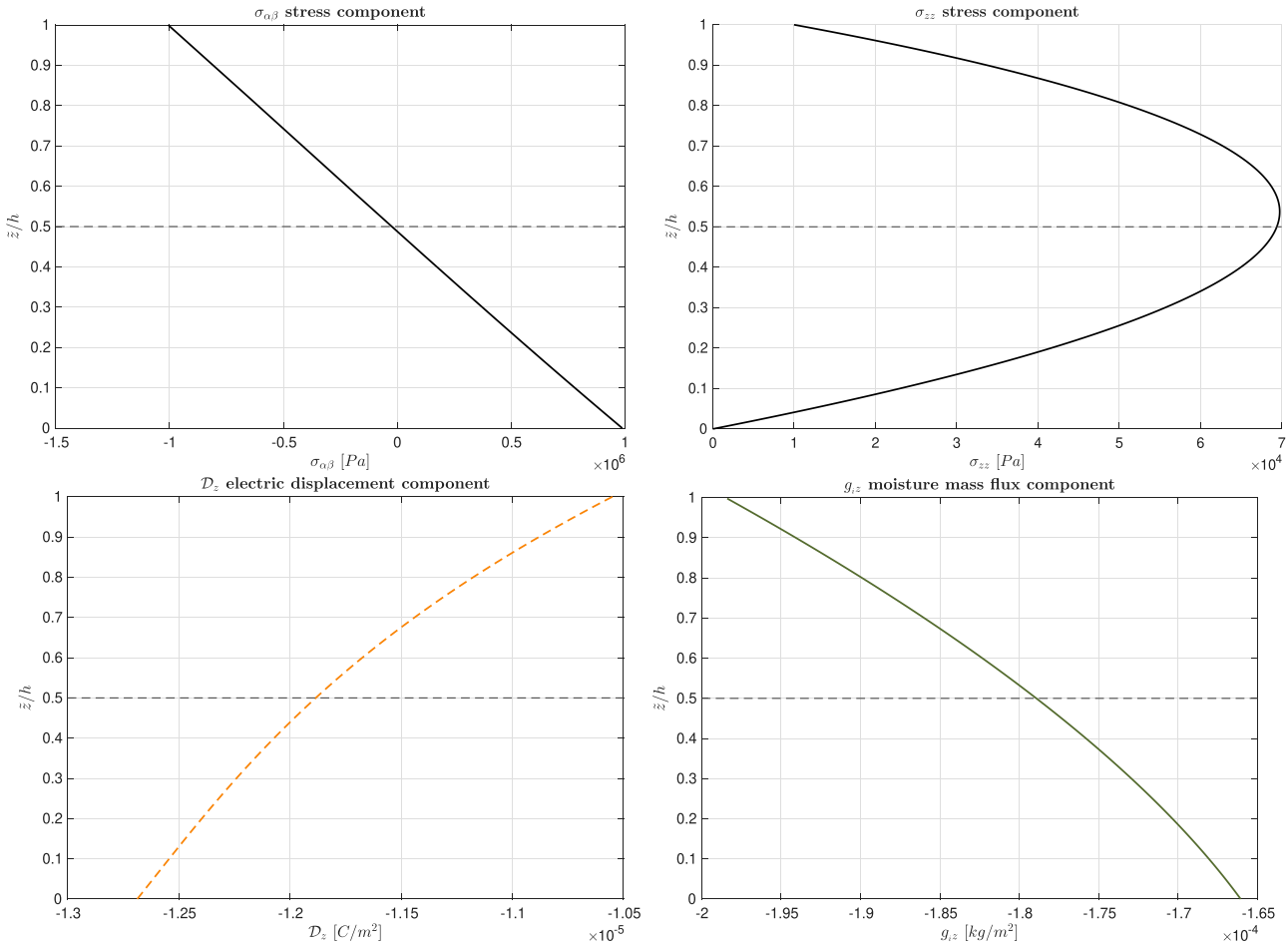

Figure 12 Benchmark B4, 3D-u-ϕ-$\mathcal{M}$ graphical trends along the thickness direction for the simply-supported multilayered spherical shell in sensor closed circuit configuration ($\bar{P}_{z_t} = 10000\,Pa$, $\bar{P}_{z_b} = 0\,Pa$, $\bar{\Phi}_t = 0\,A$, $\bar{\Phi}_b = 0\,A$, $\bar{\mathcal{M}}_t = 1.5\,kg/m^3$, $\bar{\mathcal{M}}_b = 0.5\,kg/m^3$) for $R_\alpha/h = 10$.

the problem are the amplitudes U^k, V^k, W^k, Φ^k, and M^k, together with their first derivatives with respect to z. The resulting first-order system can be written as

$$A_8^k U_{,z}^k = A_8^k U_{,z}^k, \tag{39}$$

$$A_{16}^k V_{,z}^k = A_{16}^k V_{,z}^k, \tag{40}$$

$$P_1^k W_{,z}^k = P_1^k W_{,z}^k, \tag{41}$$

$$P_1^k \Phi_{,z}^k = P_1^k \Phi_{,z}^k, \tag{42}$$

$$J_7^k M_{,z}^k = J_7^k M_{,z}^k. \tag{43}$$

$$\begin{aligned} A_8^k U_{,zz}^k = &-A_1^k U^k - A_2^k V^k - A_3^k W^k - A_4^k \Phi^k - J_1^k M^k - A_5^k U_{,z}^k \\ &- A_6^k W_{,z}^k + -A_7^k \Phi_{,z}^k, \end{aligned} \tag{44}$$

$$\begin{aligned} A_{16}^k V_{,zz}^k = &-A_9^k U^k - A_{10}^k V^k - A_{11}^k W^k - A_{12}^k \Phi^k - J_2^k M^k \\ &- A_{13}^k V_{,z}^k - A_{14}^k W_{,z}^k + -A_{15}^k \Phi_{,z}^k, \end{aligned} \tag{45}$$

$$\begin{aligned} P_1^k W_{,zz}^k = &-P_2^k U^k - P_3^k V^k - P_4^k W^k - P_5^k \Phi^k - PP_1^k M^k - P_7^k U_{,z}^k \\ &- P_8^k V_{,z}^k - P_9^k W_{,z}^k + -P_{10}^k \Phi_{,z}^k - PP_2^k M_{,z}^k, \end{aligned} \tag{46}$$

$$\begin{aligned} P_1^k \Phi_{,zz}^k = &-P_{12}^k U^k - P_{13}^k V^k - P_{14}^k W^k - P_{15}^k \Phi^k - PP_3^k M^k \\ &- P_{17}^k U_{,z}^k - P_{18}^k V_{,z}^k - P_{19}^k W_{,z}^k + -P_{20}^k \Phi_{,z}^k - PP_2^k M_{,z}^k, \end{aligned} \tag{47}$$

$$J_7^k M_{,zz}^k = -J_6^k M^k. \tag{48}$$

Thanks to the order-reduction procedure, the first derivatives of the five primary variables, namely $U_{,z}^k(z)$, $V_{,z}^k(z)$, $W_{,z}^k(z)$, $\Phi_{,z}^k(z)$, and $M_{,z}^k(z)$, are introduced as additional unknowns. Terms P_i^k and PP_i^k are a multiplication of A_i^k terms and A_i^k with J_i^k terms, respectively. Consequently, the final state-space system consists of ten first-order differential equations. From this point onward, the formulation is referred to a generic mathematical layer j. The resulting first-order system can be conveniently expressed in the following matrix form:

$$\boldsymbol{D}^j \boldsymbol{X}_{,z}^j = \boldsymbol{A}^j \boldsymbol{X}^j \quad \Rightarrow \quad \boldsymbol{X}_{,z}^j = \boldsymbol{A}^{*j} \boldsymbol{X}^j, \quad \text{where} \quad \boldsymbol{A}^{*j} = \left(\boldsymbol{D}^j\right)^{-1} \boldsymbol{A}^j. \tag{49}$$

Here, $\boldsymbol{X}^j$ denotes the 10×1 state vector, whereas $\boldsymbol{X}_{,z}^j$ is its derivative with respect to the thickness coordinate z. The matrices $\boldsymbol{D}^j$ and $\boldsymbol{A}^j$ are the corresponding 10×10 coefficient matrices, while $\boldsymbol{A}^{*j}$ is the resulting state matrix. Owing to its constant coefficients within each mathematical layer, Eq. (49)

Downloaded from academic.oup.com/jom/article/doi/10.1093/jom/ufag025/8845483 by Politecnico di Torino user on 30 September 2026

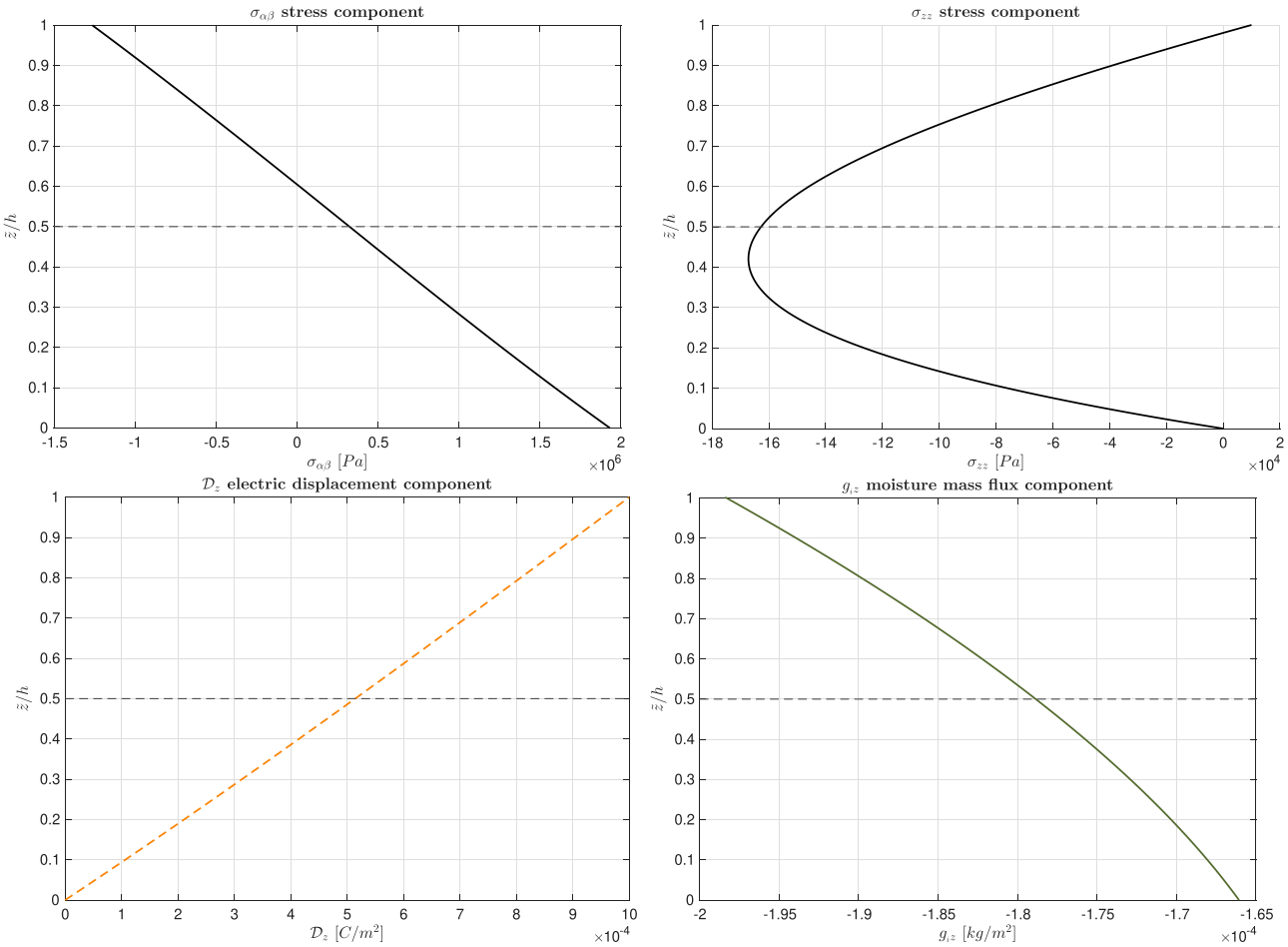

Figure 13 Benchmark B4, 3D-u-ϕ-$\mathcal{M}$ graphical trends along the thickness direction for the simply-supported multilayered spherical shell in sensor open circuit configuration ($\bar{P}_{z_t} = 10000\,Pa$, $\bar{P}_{z_b} = 0\,Pa$, $\bar{\mathcal{D}}_{z_t} = 0.001\,C/m^2$, $\bar{\mathcal{D}}_{z_b} = 0\,C/m^2$, $\bar{\mathcal{M}}_t = 1.5\,kg/m^3$, $\bar{\mathcal{M}}_b = 0.5\,kg/m^3$) for $R_\alpha/h = 10$.

admits the exponential matrix solution

$$\boldsymbol{X}^j(h_j) = \boldsymbol{A}^{**j}\boldsymbol{X}^j(0) = \left[\sum_{i=0}^{N} \frac{\left(\boldsymbol{A}^{*j}\right)^i}{i!} h_j^i\right]\boldsymbol{X}^j(0). \tag{50}$$

Eq. (50) establishes the relationship between the bottom surface ($\tilde{z}_j = 0$) and the top surface ($\tilde{z}_j = h_j$) of the generic mathematical layer j. In order to accurately reproduce the three-dimensional response of HEE smart structures, a layer-wise description is adopted. This formulation enforces the continuity of the primary variables together with the continuity of the transverse stress, electric displacement, and moisture flux components across the interfaces separating two adjacent mathematical layers ($j-1$ and j). Accordingly, the following interlaminar continuity conditions are imposed:

$$u_b^j = u_t^{j-1}, \quad v_b^j = v_t^{j-1}, \quad w_b^j = w_t^{j-1}, \quad \phi_b^j = \phi_t^{j-1},$$
$$\mathcal{M}_b^j = \mathcal{M}_t^{j-1}, \tag{51}$$

$$\sigma_{\alpha z_b}^j = \sigma_{\alpha z_t}^{j-1}, \quad \sigma_{\beta z_b}^j = \sigma_{\beta z_t}^{j-1}, \quad \sigma_{zz_b}^j = \sigma_{zz_t}^{j-1}, \quad \mathcal{D}_{z_b}^j = \mathcal{D}_{z_t}^{j-1},$$
$$g_{z_b}^j = g_{z_t}^{j-1}. \tag{52}$$

The continuity conditions given by Eqs. (51) and (52) can be rewritten explicitly in terms of the state variables as

$$U_b^j = U_t^{j-1}, \tag{53}$$
$$V_b^j = V_t^{j-1}, \tag{54}$$
$$W_b^j = W_t^{j-1}, \tag{55}$$
$$\Phi_b^j = \Phi_t^{j-1}, \tag{56}$$
$$M_b^j = M_t^{j-1}, \tag{57}$$

$$\frac{C_{55}^j}{H_{\alpha_b}^j}\bar{\alpha}W_b^j + C_{55}^j U_{,z_b}^j - \frac{C_{55}^j}{H_{\alpha_b}^j R_\alpha}U_b^j + \frac{e_{15}^j}{H_{\alpha_b}^j}\bar{\alpha}\Phi_b^j$$
$$= +\frac{C_{55}^{j-1}}{H_{\alpha_t}^{j-1}}\bar{\alpha}W_t^{j-1} + C_{55}^{j-1}U_{,z_t}^{j-1} - \frac{C_{55}^{j-1}}{H_{\alpha_t}^{j-1}R_\alpha}U_t^{j-1}$$
$$+\frac{e_{15}^{j-1}}{H_{\alpha_t}^{j-1}}\bar{\alpha}\Phi_t^{j-1}, \tag{58}$$

Downloaded from academic.oup.com/jom/article/doi/10.1093/jom/ufag025/8845483 by Politecnico di Torino user on 30 September 2026

$$\frac{C_{44}^j}{H_{\beta_b}^j}\bar{\beta}W_b^j + C_{44}^j V_{,z_b}^j - \frac{C_{44}^j}{H_{\beta_b}^j R_\beta}V_b^j + \frac{e_{24}^j}{H_{\beta_b}^j}\bar{\beta}\Phi_b^j$$
$$= +\frac{C_{44}^{j-1}}{H_{\beta_t}^{j-1}}\bar{\beta}W_t^{j-1} + C_{44}^{j-1}V_{,z_t}^{j-1} - \frac{C_{44}^{j-1}}{H_{\beta_t}^{j-1}R_\beta}V_t^{j-1}$$
$$+ \frac{e_{24}^{j-1}}{H_{\beta_t}^{j-1}}\bar{\beta}\Phi_t^{j-1}, \tag{59}$$

$$-\frac{C_{13}^j}{H_{\alpha_b}^j}\bar{\alpha}U_b^j + \frac{C_{13}^j}{H_{\alpha_b}^j R_\alpha}W_b^j - \frac{C_{23}^j}{H_{\beta_b}^j}\bar{\beta}V_b^j + \frac{C_{23}^j}{H_{\beta_b}^j R_\beta}W_b^j$$
$$-\xi_{33}^j M_b^j + C_{33}^j W_{,z_b}^j + e_{33}^j \Phi_{,z_b}^j = -\frac{C_{13}^{j-1}}{H_{\alpha_t}^{j-1}}\bar{\alpha}U_t^{j-1} + \frac{C_{13}^{j-1}}{H_{\alpha_t}^{j-1}R_\alpha}W_t^{j-1}$$
$$-\frac{C_{23}^{j-1}}{H_{\beta_t}^{j-1}}\bar{\beta}V_t^{j-1} + \frac{C_{23}^{j-1}}{H_{\beta_t}^{j-1}R_\beta}W_t^{j-1} - \xi_{33}^{j-1}M_t^{j-1} + +C_{33}^{j-1}W_{,z_t}^{j-1}$$
$$+ e_{33}^{j-1}\Phi_{,z_t}^{j-1}, \tag{60}$$

$$-\frac{e_{31}^j}{H_{\alpha_b}^j}\bar{\alpha}U_b^j + \frac{e_{31}^j}{H_{\alpha_b}^j R_\alpha}W_b^j - \frac{e_{32}^j}{H_{\beta_b}^j}\bar{\beta}V_b^j + \frac{e_{32}^j}{H_{\beta_b}^j R_\beta}W_b^j + s_3^j M_b^j$$
$$+ e_{33}^j W_{,z_b}^j - \epsilon_{33}^j \Phi_{,z_b}^j = -\frac{e_{31}^{j-1}}{H_{\alpha_t}^{j-1}}\bar{\alpha}U_t^j + \frac{e_{31}^{j-1}}{H_{\alpha_t}^{j-1}R_\alpha}W_t^j - \frac{e_{32}^{j-1}}{H_{\beta_t}^{j-1}}\bar{\beta}V_t^j$$
$$+ \frac{e_{32}^{j-1}}{H_{\beta_t}^{j-1}R_\beta}W_t^j + s_3^{j-1}M_t^{j-1} + +e_{33}^{j-1}W_{,z_t}^{j-1} - \epsilon_{33}^{j-1}\Phi_{,z_t}^{j-1}, \tag{61}$$

$$-D_{33}^j M_{,z_b}^j = -D_{33}^{j-1}M_{,z_t}^{j-1}. \tag{62}$$

The interlaminar continuity conditions expressed by Eqs. (53)–(62) can be assembled into the following compact matrix relation:

$$\boldsymbol{X}_b^j = \boldsymbol{T}^{j,j-1}\boldsymbol{X}_t^{j-1}, \tag{63}$$

where the state vector at the bottom (b) of the jth mathematical layer is related to the state vector at the top (t) of the adjacent $(j-1)$th layer through the 10×10 transfer matrix $\boldsymbol{T}^{j,j-1}$:

$$\boldsymbol{T}^{j,j-1} = \begin{bmatrix} 1 & 0 & 0 & 0 & 0 & 0 & 0 & 0 & 0 & 0 \\ 0 & 1 & 0 & 0 & 0 & 0 & 0 & 0 & 0 & 0 \\ 0 & 0 & 1 & 0 & 0 & 0 & 0 & 0 & 0 & 0 \\ 0 & 0 & 0 & 1 & 0 & 0 & 0 & 0 & 0 & 0 \\ 0 & 0 & 0 & 0 & 1 & 0 & 0 & 0 & 0 & 0 \\ T_1 & 0 & T_2 & T_3 & 0 & T_4 & 0 & 0 & 0 & 0 \\ 0 & T_5 & T_6 & T_7 & 0 & 0 & T_8 & 0 & 0 & 0 \\ T_9 & T_{10} & T_{11} & 0 & \tau_1 & 0 & 0 & T_{12} & T_{13} & 0 \\ T_{14} & T_{15} & T_{16} & 0 & \tau_2 & 0 & 0 & T_{17} & T_{18} & 0 \\ 0 & 0 & 0 & 0 & 0 & 0 & 0 & 0 & 0 & \tau_3 \end{bmatrix}^{j,j-1}. \tag{64}$$

By recursively combining Eq. (63) with Eq. (50), from the top surface ($\tilde{z}_M = h_M$) of the last (M-th) mathematical layer to the bottom surface ($\tilde{z}_1 = 0$) of the first layer, the following global relation is obtained:

$$\boldsymbol{X}^M(h_M) = \boldsymbol{A}^{**M}\boldsymbol{T}^{M,M-1}\ldots\boldsymbol{T}^{2,1}\boldsymbol{A}^{**1}\boldsymbol{X}^1(0) = \boldsymbol{H}_m\boldsymbol{X}^1(0), \tag{65}$$

where $\boldsymbol{H}_m$ denotes the *multilayered matrix*, which incorporates all the structural information associated with the multilayered configuration, including the multifield material properties, the geometrical parameters, and the curvature effects along the thickness coordinate z. Regardless of the number of mathematical layers adopted to discretize the thickness, the *multilayered matrix* $\boldsymbol{H}_m$ always has dimensions 10×10. Consequently, the proposed formulation provides a computationally efficient solution while preserving the full three-dimensional layer-wise description.

At the final stage of the solution procedure, the boundary conditions are enforced at the top and bottom surfaces of the structure. Depending on the considered electromechanical configuration, the prescribed quantities are expressed in terms of transverse pressure, moisture content, and either electric potential or transverse electric displacement. Three different loading configurations are considered, namely the actuator configuration, the sensor closed-circuit configuration, and the sensor open-circuit configuration:

$$\sigma_{zz} = 0,\ \sigma_{\alpha z} = 0,\ \sigma_{\beta z} = 0,\ \mathcal{M} = \bar{\mathcal{M}},\ \phi = \bar{\phi} \text{ for } z = \pm h/2 \quad \text{(actuator configuration)}, \tag{66}$$

$$\sigma_{zz} = \bar{p}_z,\ \sigma_{\alpha z} = 0,\ \sigma_{\beta z} = 0,\ \mathcal{M} = \bar{\mathcal{M}},\ \phi = 0 \text{ for } z = \pm h/2 \quad \text{(sensor closed-circuit configuration)}, \tag{67}$$

$$\sigma_{zz} = \bar{p}_z,\ \sigma_{\alpha z} = 0,\ \sigma_{\beta z} = 0,\ \mathcal{M} = \bar{\mathcal{M}},\ \mathcal{D}_z = \bar{\mathcal{D}}_z \text{ for } z = \pm h/2 \quad \text{(sensor open-circuit configuration)}, \tag{68}$$

where the overbar denotes a prescribed boundary value. By substituting the constitutive relations given in Eqs. (7)–(9) together with the harmonic expansions defined in Eqs. (24)–(26), the above boundary conditions can be rewritten in compact matrix form as follows:

$$\boldsymbol{B}_b^1\boldsymbol{X}^1(0) = \boldsymbol{P}_b, \tag{69}$$

$$\boldsymbol{B}_t^M\boldsymbol{X}^M(h_M) = \boldsymbol{P}_t, \tag{70}$$

where $\boldsymbol{B}_b^1$ and $\boldsymbol{B}_t^M$ denote the 5×10 boundary-condition matrices associated with the bottom surface (b) of the first layer and the top surface (t) of the last layer, respectively. Likewise, $\boldsymbol{P}_b$ and $\boldsymbol{P}_t$ are the corresponding 5×1 loading vectors prescribed at the bottom and top surfaces of the multilayered structure. By introducing Eq. (65) into Eq. (70), the latter becomes

$$\boldsymbol{B}_t^M\boldsymbol{H}_m\boldsymbol{X}^1(0) = \boldsymbol{P}_t. \tag{71}$$

Combining Eqs. (71) and (69) yields the final linear algebraic system

$$\boldsymbol{E}\boldsymbol{X}^1(0) = \boldsymbol{P}, \tag{72}$$

where

$$\boldsymbol{E} = \begin{bmatrix} \boldsymbol{B}_t^M\boldsymbol{H}_m \\ \boldsymbol{B}_b^1 \end{bmatrix}, \qquad \boldsymbol{P} = \begin{Bmatrix} \boldsymbol{P}_t \\ \boldsymbol{P}_b \end{Bmatrix}. \tag{73}$$

Solving Eq. (72) provides the state vector at the bottom surface of the multilayered structure, including the primary variables and their first derivatives with respect to the thickness coordinate z. The complete three-dimensional solution

Downloaded from academic.oup.com/jom/article/doi/10.1093/jom/ufag025/8845483 by Politecnico di Torino user on 30 September 2026

through the thickness is subsequently recovered by recursively applying Eqs. (50)–(63). Consequently, the displacement components, electric potential, and moisture content distributions are directly obtained, whereas the corresponding strains, stresses, moisture fluxes, and electric displacement components are evaluated through the constitutive relations in Eqs. (7)–(9).

3. Results

The numerical results presented in this section are used to assess the accuracy and the predictive capabilities of the proposed three-dimensional coupled HEE formulation. Comparisons with refined HEE models available in the literature are first performed to validate the proposed approach. All the numerical results have been obtained using an in-house Matlab code implementing the formulation described in Section 2. Throughout this section, the proposed formulation is referred to as the 3D-u-ϕ-$\mathcal{M}$ model, emphasizing its three-dimensional nature and the adopted set of primary variables, namely the displacement components (u), the electric potential (ϕ), and the moisture content ($\mathcal{M}$).

The section is organized into two parts. First, a set of assessemnts is considered to verify the accuracy of the proposed 3D-u-ϕ-$\mathcal{M}$ model through comparisons with reference solutions available in the literature. Subsequently, new HEE benchmark problems are presented by considering different structural geometries and loading boundary conditions.

3.1. Assessments

In the present subsection, two assessment cases are presented. The first assessment deals with a multilayered plate, whereas the second one considers a multilayered shell. Both structures are simply supported along the four edges. The adopted stacking sequence is *Adaptive Wood/Soft Adaptive Wood/Adaptive Wood*, where each outer *Adaptive Wood* layer has a thickness equal to $0.3h$, while the *Soft Adaptive Wood* core occupies the remaining $0.4h$, with h denoting the total thickness of the structure.

The elastic, electric, and hygrometric material properties adopted in the two assessment cases are reported in Table 1. The numerical results obtained with the proposed 3D-u-ϕ-$\mathcal{M}$ model are computed by employing $M = 300$ mathematical layers and an exponential matrix expansion of order $N = 3$. Convergence results attesting the correctness in depicting all the possible three-dimensional effects by considering these two values are proposed in [52]. The reference solutions are extracted from the graphical results reported in [51] at the in-plane position ($x = 0.25a$, $y = 0.25b$). The comparison is performed against the Equivalent Layerwise fourth-order axiomatic HEE model (ELDZL4) presented in [51]. Since the hygrovelectric coupling coefficient is equal to zero for both *Adaptive Wood* and *Soft Adaptive Wood*, the direct hygro−electric coupling effect is absent in the considered assessment cases.

The first assessment (A1) considers a multilayered simply-supported plate. The geometrical parameters together with the loading boundary conditions prescribed at the outer surfaces, in terms of mechanical pressure, electric potential, and moisture concentration, are summarized in the first column of Table 2. The comparison between the ELDZL4 HEE model and the proposed 3D-u-ϕ-$\mathcal{M}$ model is reported in Table 3. An excellent agreement is observed for the displacement components, electric potential, moisture concentration, transverse normal stress, and in-plane normal electric displacement components. The small discrepancies can be mainly attributed to two factors: the digitization of the graphical results reported in [51] and the comparison between an exact three-dimensional formulation and a two-dimensional numerical model. This assessment confirms the capability of the proposed formulation to accurately reproduce the coupled HEE response, including the effects associated with the thickness direction and the multilayered configuration for flat structures.

The second assessment (A2) considers a multilayered simply-supported spherical shell. The corresponding geometrical parameters and the loading boundary conditions prescribed at the external surfaces are listed in the second column of Table 2. The assessment compares the predictions of the proposed 3D-u-ϕ-$\mathcal{M}$ formulation with those provided by the ELDZL4 HEE model presented in [51]. The comparison reported in Table 4 shows an excellent agreement for the displacement components and the transverse shear stress component, while an almost perfect correspondence is obtained for the moisture concentration and the in-plane normal electric displacement components. The small differences observed are attributable to the same two factors discussed for the first assessment (A1), namely the extraction of the reference data from graphical results and the comparison between an exact three-dimensional formulation and a two-dimensional numerical model. Therefore, the present assessment further confirms the capability of the proposed 3D formulation to accurately capture the coupled HEE response, including the thickness and material layer effects in curved multilayered structures.

The two assessment cases confirm that the selection of $M = 300$ mathematical layers and an exponential matrix expansion of order $N = 3$ provides accurate results for both flat and curved structures in the framework of the coupled HEE analysis. Therefore, these two numerical parameters are kept unchanged in all the following four benchmark cases.

3.2. New benchmarks

This subsection presents four new two-layered benchmark cases involving simply-supported two-layered plates, cylinders, cylindrical panels, and spherical shells. The geometrical parameters together with the adopted reference system for each structural configuration are illustrated in Fig. 1. All the analyzed structures are characterized by a two-layered $0°/90°$ stacking sequence made of the HEE Material. Each HEE material laminae has a thickness equal to $0.5h$ by considering as h the total thickness of the geometry. The corresponding elastic, electric, and hygrometric material properties are reported in Table 5. The *HEE Material* was originally introduced by Tariq *et al.* [38]. For each benchmark case, three different loading boundary conditions are considered in order to reproduce actuator and sensor operating configurations.

Downloaded from academic.oup.com/jom/article/doi/10.1093/jom/ufag025/8845483 by Politecnico di Torino user on 30 September 2026

Table 9 Benchmark B1, simply-supported multilayered rectangular plate in sensor open circuit configuration ($\bar{P}_{z_t} = 10000\,Pa$, $\bar{P}_{z_b} = 0\,Pa$, $\bar{\mathcal{D}}_{z_t} = 0.001\,C/m^2$, $\bar{\mathcal{D}}_{z_b} = 0\,C/m^2$, $\bar{\mathcal{M}}_t = 1.5\,kg/m^3$, $\bar{\mathcal{M}}_b = 0.5\,kg/m^3$).

a/h	2	4	10	50	100
		$u\,[10^{-6}\,m]$ $(\tilde{z}/h = 0.00)$			
	−10.346	−9.5777	−7.7601	−0.7395	19.731
		$w\,[10^{-5}\,m]$ $(\tilde{z}/h = 0.75)$			
	1.0290	0.5478	−1.7183	8.2693	146.49
		$\phi\,[10^{6}\,A]$ $(\tilde{z}/h = 0.25)$			
	−0.3091	−1.3736	−4.5474	−24.057	−48.200
		$\mathcal{M}\,[kg/m^3]$ $(\tilde{z}/h = 0.25)$			
	0.2908	0.5463	0.7086	0.7483	0.7496
		$\sigma_{\alpha\beta}\,[10^{5}\,Pa]$ $(\tilde{z}/h = 0.75)$			
	−4.7412	−8.6550	−11.229	−14.801	−24.106
		$\sigma_{zz}\,[10^{4}\,Pa]$ $(\tilde{z}/h = 0.75)$			
	−41.399	−6.1965	0.5798	0.8432	0.8437
		$\mathcal{D}_z\,[10^{-4}\,C/m^2]$ $(\tilde{z}/h = 0.25)$			
	0.6737	1.6886	2.3361	2.4933	2.4984
		$g_z\,[10^{-5}\,kg/m^2]$ $(\tilde{z}/h = 1.00)$			
	−94.476	−90.646	−115.68	−455.32	−902.66

Results obtained via the 3D-u-ϕ-$\mathcal{M}$ model. $\tilde{z}/h$ goes from 0 (bottom) to 1 (top).

Table 10 Benchmark B2, simply-supported multilayered cylinder in actuator configuration ($\bar{P}_{z_t} = 0\,Pa$, $\bar{P}_{z_b} = 0\,Pa$, $\bar{\Phi}_t = 1 \cdot 10^8\,A$, $\bar{\Phi}_b = 0\,A$, $\bar{\mathcal{M}}_t = 1.5\,kg/m^3$, $\bar{\mathcal{M}}_b = 0.5\,kg/m^3$).

R_α/h	2	4	10	50	100
		$v\,[10^{-3}\,m]$ $(\tilde{z}/h = 0.25)$			
	−0.2523	−0.5148	−1.2021	−6.1592	−12.402
		$w\,[10^{-4}\,m]$ $(\tilde{z}/h = 0.75)$			
	10.945	19.142	46.446	221.76	438.19
		$\phi\,[10^{7}\,A]$ $(\tilde{z}/h = 0.25)$			
	1.7683	2.2886	2.4698	2.5001	2.5004
		$\mathcal{M}\,[kg/m^3]$ $(\tilde{z}/h = 0.50)$			
	0.7303	0.9187	0.9862	0.9994	0.9999
		$\sigma_{\beta\beta}\,[10^{6}\,Pa]$ $(\tilde{z}/h = 0.75)$			
	1.2840	1.8012	3.1278	3.7245	3.7496
		$\sigma_{zz}\,[10^{3}\,Pa]$ $(\tilde{z}/h = 0.25)$			
	341.92	51.620	−8.5489	−1.9058	−0.8328
		$\mathcal{D}_z\,[10^{-4}\,C/m^2]$ $(\tilde{z}/h = 1.00)$			
	−31.813	−44.974	−97.326	−472.06	−943.15
		$g_z\,[10^{-4}\,kg/m^2]$ $(\tilde{z}/h = 1.00)$			
	−0.8440	−0.9967	−1.9159	−9.0234	−18.012

Results are obtained via the 3D-u-ϕ-$\mathcal{M}$ model. $\tilde{z}/h$ goes from 0 (bottom) to 1 (top).

The actuator operating configuration is defined by the following boundary conditions:

$$\bar{P}_{z_t} = 0\,Pa,\ \bar{P}_{z_b} = 0\,Pa, \quad \bar{\Phi}_t = 1 \cdot 10^8\,A,\ \bar{\Phi}_b = 0\,A,$$
$$\bar{\mathcal{M}}_t = 1.5\,kg/m^3,\ \bar{\mathcal{M}}_b = 0.5\,kg/m^3. \tag{74}$$

The sensor closed-circuit operating configuration is characterized by:

$$\bar{P}_{z_t} = 10000\,Pa,\ \bar{P}_{z_b} = 0\,Pa, \quad \bar{\Phi}_t = 0\,A,\ \bar{\Phi}_b = 0\,A,$$
$$\bar{\mathcal{M}}_t = 1.5\,kg/m^3,\ \bar{\mathcal{M}}_b = 0.5\,kg/m^3. \tag{75}$$

Finally, the sensor open-circuit operating configuration is prescribed as:

$$\bar{P}_{z_t} = 10000\,Pa,\ \bar{P}_{z_b} = 0\,Pa, \quad \bar{\mathcal{D}}_{z_t} = 0.001\,C/m^2,$$
$$\bar{\mathcal{D}}_{z_b} = 0\,C/m^2, \quad \bar{\mathcal{M}}_t = 1.5\,kg/m^3,\ \bar{\mathcal{M}}_b = 0.5\,kg/m^3. \tag{76}$$

The subscripts t and b identify the top and bottom surfaces of the multilayered structure, respectively.

The first benchmark (B1) focuses on a simply-supported plate. The corresponding geometrical parameters and half-wave numbers are listed in the first column of Table 6. Numerical results for the displacement components u and w, the electric potential ϕ, the moisture content $\mathcal{M}$, the stress components $\sigma_{\alpha\beta}$ and σ_{zz}, the transverse electric displacement $\mathcal{D}_z$, and the moisture flux g_z are reported in Tables 7–9 for the actuator, sensor closed-circuit, and sensor open-circuit operating configurations, respectively. The results are presented for different thickness ratios, ranging from thick ($a/h = 2$) to thin ($a/h = 100$) plates, and at selected through-the-thickness positions $\tilde{z}/h$.

The through-the-thickness distributions of the primary variables u, w, ϕ, and $\mathcal{M}$ are illustrated in Fig. 2 for the moderately thick case ($a/h = 4$) under the actuator operating configuration. The corresponding secondary variables $\sigma_{\alpha\beta}$, σ_{zz}, $\mathcal{D}_z$, and g_z are reported in Fig. 3 for the sensor closed-circuit configuration and in Fig. 4 for the sensor open-circuit configuration.

For all the considered loading configurations, the characteristic features of the coupled HEE response are clearly identified. The classical zigzag behavior appears as slope discontinuities at the interface between the two laminae, while the thickness and material layer effects are accurately captured throughout the thickness. Moreover, the prescribed boundary conditions are fully satisfied at the external surfaces of the plate. The continuity requirements at the layer interface are also fulfilled for all the loading configurations. This behavior is confirmed by the continuous through-the-thickness distributions of all the reported variables, which do not exhibit artificial jumps across the interface. Finally, the mutual coupling among the hygrometric, electric, and elastic fields is clearly highlighted, since all the corresponding field variables exhibit nonzero distributions along the thickness direction.

The second benchmark (B2) examines a simply-supported cylindrical structure. The corresponding geometrical parameters and half-wave numbers are reported in the second column of Table 6. Numerical results for the displacement components v and w, the electric potential ϕ, the moisture content $\mathcal{M}$, the stress components $\sigma_{\beta\beta}$ and σ_{zz}, the transverse electric displacement $\mathcal{D}_z$, and the moisture flux g_z are collected in Tables 10–12 for the actuator, sensor closed-circuit, and sensor open-circuit operating configurations, respectively. The tabulated results cover thickness ratios ranging from thick ($R_\alpha/h = 2$) to thin ($R_\alpha/h = 100$) cylinders and are reported at selected through-the-thickness positions $\tilde{z}/h$.

The through-the-thickness distributions corresponding to the actuator operating configuration are illustrated in Fig. 5. Figures 6 and 7 show the corresponding distributions for the sensor closed-circuit and sensor open-circuit operating con-

Downloaded from academic.oup.com/jom/article/doi/10.1093/jom/ufag025/8845483 by Politecnico di Torino user on 30 September 2026

Table 11 Benchmark B2, simply-supported multilayered cylinder in sensor closed circuit configuration ($\bar{P}_{z_t} = 10000\,Pa$, $\bar{P}_{z_b} = 0\,Pa$, $\bar{\Phi}_t = 0\,A$, $\bar{\Phi}_b = 0\,A$, $\bar{\mathcal{M}}_t = 1.5\,kg/m^3$, $\bar{\mathcal{M}}_b = 0.5\,kg/m^3$).

R_α/h	2	4	10	50	100
		$v\,[10^{-4}\,m]$ $(\tilde{z}/h = 0.25)$			
	−1.2800	−1.3559	−1.7374	−2.2125	−2.1559
		$w\,[10^{-4}\,m]$ $(\tilde{z}/h = 0.75)$			
	5.0427	7.3361	9.5085	10.545	11.823
		$\phi\,[10^4\,A]$ $(\tilde{z}/h = 0.25)$			
	5.7655	4.2709	−0.5075	−0.6472	−0.3586
		$\mathcal{M}\,[kg/m^3]$ $(\tilde{z}/h = 0.50)$			
	0.7303	0.9187	0.9862	0.9994	0.9999
		$\sigma_{\beta\beta}\,[10^5\,Pa]$ $(\tilde{z}/h = 0.75)$			
	3.5920	5.2405	−2.6691	−12.997	−13.954
		$\sigma_{zz}\,[10^4\,Pa]$ $(\tilde{z}/h = 0.25)$			
	−8.4222	0.7757	3.7593	1.4082	0.8531
		$\mathcal{D}_z\,[10^{-5}\,C/m^2]$ $(\tilde{z}/h = 1.00)$			
	−0.7221	−0.8735	−1.2186	−1.4782	−1.6857
		$g_z\,[10^{-4}\,kg/m^2]$ $(\tilde{z}/h = 1.00)$			
	−0.8440	−0.9967	−1.9159	−9.0234	−18.012

Results are obtained via the 3D-u-ϕ-$\mathcal{M}$ model. $\tilde{z}/h$ goes from 0 (bottom) to 1 (top).

Table 12 Benchmark B2, simply-supported multilayered cylinder in sensor open circuit configuration ($\bar{P}_{z_t} = 10000\,Pa$ $\bar{P}_{z_b} = 0\,Pa$, $\bar{\mathcal{D}}_{z_t} = 0.001\,C/m^2$, $\bar{\mathcal{D}}_{z_b} = 0\,C/m^2$, $\bar{\mathcal{M}}_t = 1.5\,kg/m^3$, $\bar{\mathcal{M}}_b = 0.5\,kg/m^3$).

R_α/h	2	4	10	50	100
		$v\,[10^{-4}\,m]$ $(\tilde{z}/h = 0.25)$			
	−1.3109	−1.0260	−0.7804	−1.2195	−1.6758
		$w\,[10^{-4}\,m]$ $(\tilde{z}/h = 0.75)$			
	2.5231	3.5354	6.2362	12.296	18.410
		$\phi\,[10^8\,A]$ $(\tilde{z}/h = 0.25)$			
	−0.1627	−0.4046	−1.0799	−5.4694	−10.944
		$\mathcal{M}\,[kg/m^3]$ $(\tilde{z}/h = 0.50)$			
	0.7303	0.9187	0.9862	0.9994	0.9999
		$\sigma_{\beta\beta}\,[10^6\,Pa]$ $(\tilde{z}/h = 0.75)$			
	0.2601	1.2524	1.7496	2.0409	2.7730
		$\sigma_{zz}\,[10^5\,Pa]$ $(\tilde{z}/h = 0.25)$			
	−3.0261	−1.2511	−0.3129	−0.0032	0.0137
		$\mathcal{D}_z\,[10^{-4}\,C/m^2]$ $(\tilde{z}/h = 0.25)$			
	1.8403	2.3230	2.4798	2.5019	2.5013
		$g_z\,[10^{-4}\,kg/m^2]$ $(\tilde{z}/h = 1.00)$			
	−0.8440	−0.9967	−1.9159	−9.0234	−18.012

Results are obtained via the 3D-u-ϕ-$\mathcal{M}$ model. $\tilde{z}/h$ goes from 0 (bottom) to 1 (top).

figurations, respectively. All the graphical results refer to the moderately thick case $R_\alpha/h = 10$.

The proposed results clearly highlight the main characteristics of the coupled HEE response. The expected zigzag behavior is observed at the interface between the two laminae, where slope discontinuities arise owing to the different material properties. Moreover, the effects associated with both the structural thickness and the multilayered configuration

Table 13 Benchmark B3, simply-supported multilayered cylindrical panel in actuator configuration ($\bar{P}_{z_t} = 0\,Pa$, $\bar{P}_{z_b} = 0\,Pa$, $\bar{\Phi}_t = 1 \cdot 10^8\,A$, $\bar{\Phi}_b = 0\,A$, $\bar{\mathcal{M}}_t = 1.5\,kg/m^3$, $\bar{\mathcal{M}}_b = 0.5\,kg/m^3$).

R_α/h	2	4	10	50	100
		$u\,[10^{-4}\,m]$ $(\tilde{z}/h = 0.75)$			
	−7.7402	−10.028	−21.347	−238.92	−852.71
		$w\,[10^{-4}\,m]$ $(\tilde{z}/h = 0.50)$			
	8.7569	12.479	10.001	−429.13	−2002.9
		$\phi\,[10^7\,A]$ $(\tilde{z}/h = 0.25)$			
	1.8740	2.3175	2.4654	2.4931	2.4938
		$\mathcal{M}\,[kg/m^3]$ $(\tilde{z}/h = 0.50)$			
	0.7708	0.9327	0.9886	0.9995	0.9999
		$\sigma_{\alpha\alpha}\,[10^6\,Pa]$ $(\tilde{z}/h = 0.75)$			
	0.9786	0.3291	−1.3335	−11.757	−24.693
		$\sigma_{zz}\,[10^4\,Pa]$ $(\tilde{z}/h = 0.25)$			
	5.5081	4.7792	8.4426	9.5868	9.6500
		$\mathcal{D}_z\,[10^{-4}\,C/m^2]$ $(\tilde{z}/h = 1.00)$			
	−27.651	−42.828	−95.975	−468.57	−936.41
		$g_z\,[10^{-4}\,kg/m^2]$ $(\tilde{z}/h = 1.00)$			
	−0.7094	−0.9315	−1.8926	−9.0193	−18.010

Results are obtained via the 3D-u-ϕ-$\mathcal{M}$ model. $\tilde{z}/h$ goes from 0 (bottom) to 1 (top).

are accurately captured, as expected for a moderately thick cylindrical shell. The prescribed loading boundary conditions are correctly satisfied for each operating configuration, while the interaction among the hygrometric, electric, and elastic fields demonstrates the fully coupled nature of the present formulation. Finally, the interlaminar continuity conditions are fulfilled for all the reported variables (v, w, ϕ, $\mathcal{M}$, σ_{zz}, $\mathcal{D}_z$, and g_z), as confirmed by the absence of artificial discontinuities across the layer interface.

The third benchmark (B3) considers a simply-supported multilayered cylindrical panel. The corresponding geometrical parameters are reported in the third column of Table 6. Tables 13–15 summarize the numerical results obtained for thickness ratios ranging from $R_\alpha/h = 2$ to $R_\alpha/h = 100$ under the three loading boundary configurations. The variables u, w, ϕ, $\mathcal{M}$, $\sigma_{\alpha\alpha}$, σ_{zz}, $\mathcal{D}_z$, and g_z are reported at selected through-the-thickness positions $\tilde{z}/h$.

Figure 8 illustrates the distributions of the secondary variables $\sigma_{\alpha\alpha}$, σ_{zz}, $\mathcal{D}_z$, and g_z for the actuator configuration considering the thickness ratio $R_\alpha/h = 50$. The corresponding distributions of the primary variables u, w, ϕ, and $\mathcal{M}$ are presented in Fig. 9 for the sensor closed-circuit configuration and in Fig. 10 for the sensor open-circuit configuration, both for the same thickness ratio.

The proposed through-the-thickness distributions clearly exhibit the expected zigzag behavior, characterized by slope discontinuities at the interfaces between adjacent laminae. The influence of both the multilayered configuration and the structural thickness is also correctly reproduced. Furthermore, the prescribed loading boundary conditions are fully satisfied at the external surfaces for all the investigated operating configurations: $\phi_t = 1 \cdot 10^8\,A$, $\phi_b = 0\,A$, $\mathcal{M}_t = 1.5\,kg/m^3$, $\mathcal{M}_b = 0.5\,kg/m^3$, and $\sigma_{zz_t} = \sigma_{zz_b} = 0\,Pa$ for the actuator con-

Downloaded from academic.oup.com/jom/article/doi/10.1093/jom/ufag025/8845483 by Politecnico di Torino user on 30 September 2026

Table 14 Benchmark B3, simply-supported multilayered cylindrical panel in sensor closed circuit configuration ($\bar{P}_{z_t} = 10000\,Pa$, $\bar{P}_{z_b} = 0\,Pa$, $\bar{\Phi}_t = 0\,A$, $\bar{\Phi}_b = 0\,A$, $\bar{\mathcal{M}}_t = 1.5\,kg/m^3$, $\bar{\mathcal{M}}_b = 0.5\,kg/m^3$).

R_α/h	2	4	10	50	100
		$u\,[10^{-4}\,m]$ $(\tilde{z}/h = 0.75)$			
	−3.7186	−3.2422	0.4398	152.83	1127.5
		$w\,[10^{-4}\,m]$ $(\tilde{z}/h = 0.50)$			
	1.7361	4.6083	16.729	489.59	3463.8
		$\phi\,[10^{4}\,A]$ $(\tilde{z}/h = 0.25)$			
	2.9344	1.2183	1.0034	4.4036	8.7686
		$\mathcal{M}\,[kg/m^3]$ $(\tilde{z}/h = 0.50)$			
	0.7708	0.9327	0.9886	0.9995	0.9999
		$\sigma_{\alpha\alpha}\,[10^{5}\,Pa]$ $(\tilde{z}/h = 0.75)$			
	0.4226	0.7309	3.8678	94.109	375.53
		$\sigma_{zz}\,[10^{4}\,Pa]$ $(\tilde{z}/h = 0.25)$			
	−0.1561	−0.6221	−1.4060	−7.0060	−14.030
		$\mathcal{D}_z\,[10^{-6}\,C/m^2]$ $(\tilde{z}/h = 1.00)$			
	4.8192	3.3883	2.0328	1.2707	1.2670
		$g_z\,[10^{-4}\,kg/m^2]$ $(\tilde{z}/h = 1.00)$			
	−0.7094	−0.9315	−1.8926	−9.0193	−18.010

Results are obtained via the 3D-u-ϕ-$\mathcal{M}$ model. $\tilde{z}/h$ goes from 0 (bottom) to 1 (top).

Table 15 Benchmark B3, simply-supported multilayered cylindrical panel in sensor open circuit configuration ($\bar{P}_{z_t} = 10000\,Pa$, $\bar{P}_{z_b} = 0\,Pa$, $\bar{\mathcal{D}}_{z_t} = 0.001\,C/m^2$, $\bar{\mathcal{D}}_{z_b} = 0\,C/m^2$, $\bar{\mathcal{M}}_t = 1.5\,kg/m^3$, $\bar{\mathcal{M}}_b = 0.5\,kg/m^3$).

R_α/h	2	4	10	50	100
		$u\,[10^{-3}\,m]$ $(\tilde{z}/h = 0.75)$			
	−0.2902	−0.3258	1.2076	254.12	2081.1
		$w\,[10^{-3}\,m]$ $(\tilde{z}/h = 0.50)$			
	−0.2239	−0.0352	5.5615	793.76	6368.9
		$\phi\,[10^{8}\,A]$ $(\tilde{z}/h = 0.25)$			
	−0.1966	−0.4884	−1.3068	−6.6234	−13.254
		$\mathcal{M}\,[kg/m^3]$ $(\tilde{z}/h = 0.50)$			
	0.7708	0.9327	0.9886	0.9995	0.9999
		$\sigma_{\alpha\alpha}\,[10^{6}\,Pa]$ $(\tilde{z}/h = 0.75)$			
	−0.3285	0.2717	5.2108	170.90	703.63
		$\sigma_{zz}\,[10^{5}\,Pa]$ $(\tilde{z}/h = 0.25)$			
	−0.6251	−1.2817	−2.9949	−13.863	−27.431
		$\mathcal{D}_z\,[10^{-4}\,C/m^2]$ $(\tilde{z}/h = 0.25)$			
	2.6651	2.7780	2.6541	2.5011	2.4449
		$g_z\,[10^{-4}\,kg/m^2]$ $(\tilde{z}/h = 1.00)$			
	−0.7094	−0.9315	−1.8926	−9.0193	−18.010

Results are obtained via the 3D-u-ϕ-$\mathcal{M}$ model. $\tilde{z}/h$ goes from 0 (bottom) to 1 (top).

figuration; $\phi_t = \phi_b = 0\,A$, $\mathcal{M}_t = 1.5\,kg/m^3$, $\mathcal{M}_b = 0.5\,kg/m^3$, $\sigma_{zz_t} = 10000\,Pa$, and $\sigma_{zz_b} = 0\,Pa$ for the sensor closed-circuit configuration; $\mathcal{D}_{z_t} = 0.001\,C/m^2$, $\mathcal{D}_{z_b} = 0\,C/m^2$, $\mathcal{M}_t = 1.5\,kg/m^3$, $\mathcal{M}_b = 0.5\,kg/m^3$, and $\sigma_{zz_t} = \sigma_{zz_b} = 0\,Pa$ for the sensor open-circuit configuration.

Finally, the continuity conditions at the interfaces between adjacent layers are fully satisfied, as demonstrated by the continuous through-the-thickness distributions of all the investigated variables, which do not exhibit artificial discontinuities across the physical interfaces.

Table 16 Benchmark B4, simply-supported multilayered spherical shell in actuator configuration ($\bar{P}_{z_t} = 0\,Pa$, $\bar{P}_{z_b} = 0\,Pa$, $\bar{\Phi}_t = 1 \cdot 10^8\,A$, $\bar{\Phi}_b = 0\,A$, $\bar{\mathcal{M}}_t = 1.5\,kg/m^3$, $\bar{\mathcal{M}}_b = 0.5\,kg/m^3$).

R_α/h	2	4	10	50	100
		$v\,[10^{-4}\,m]$ $(\tilde{z}/h = 0.75)$			
	−3.5467	−4.0791	−4.5756	−4.0653	−3.9110
		$w\,[10^{-4}\,m]$ $(\tilde{z}/h = 0.50)$			
	9.2695	16.325	40.076	200.46	397.30
		$\phi\,[10^{7}\,A]$ $(\tilde{z}/h = 0.75)$			
	6.0500	7.0299	7.4229	7.4989	7.5004
		$\mathcal{M}\,[kg/m^3]$ $(\tilde{z}/h = 0.50)$			
	0.6177	0.8728	0.9775	0.9991	0.9998
		$\sigma_{\alpha\beta}\,[10^{6}\,Pa]$ $(\tilde{z}/h = 0.50)$			
	−1.3587	−1.9497	−1.8650	−1.0147	−0.8552
		$\sigma_{zz}\,[10^{5}\,Pa]$ $(\tilde{z}/h = 0.75)$			
	12.598	3.0226	−0.7595	−0.4445	−0.2363
		$\mathcal{D}_z\,[10^{-4}\,C/m^2]$ $(\tilde{z}/h = 1.00)$			
	−35.073	−48.212	−99.007	−472.41	−943.31
		$g_z\,[10^{-4}\,kg/m^2]$ $(\tilde{z}/h = 1.00)$			
	−0.9768	−1.1267	−1.9839	−9.0385	−18.019

Results are obtained via the 3D-u-ϕ-$\mathcal{M}$ model. $\tilde{z}/h$ goes from 0 (bottom) to 1 (top).

The fourth benchmark (B4) investigates a simply-supported multilayered spherical shell. The corresponding geometrical parameters and half-wave numbers are reported in the fourth column of Table 6. Numerical results for the actuator, sensor closed-circuit, and sensor open-circuit operating configurations are collected in Tables 16, 17, and 18, respectively. The proposed results include the variables v, w, ϕ, $\mathcal{M}$, $\sigma_{\alpha\beta}$, σ_{zz}, $\mathcal{D}_z$, and g_z for both thick and thin spherical shells.

The through-the-thickness distributions corresponding to the actuator configuration are presented in Fig. 11 for the thickness ratio $R_\alpha/h = 10$. The analogous results for the sensor closed-circuit and sensor open-circuit operating configurations are reported in Figs 12 and 13, respectively.

For all the investigated operating configurations, the characteristic zigzag behavior is clearly observed through the slope discontinuities occurring at the interfaces between adjacent laminae. The proposed results also demonstrate the coupled HEE response, since the mechanical, electric, and hygrometric fields remain mutually coupled even when pressure loads and/or electric potentials are not directly prescribed at the external surfaces. Furthermore, the imposed loading boundary conditions are accurately satisfied at both outer surfaces of the structure. Finally, the continuity conditions across the material interfaces are correctly fulfilled, as confirmed by the continuous through-the-thickness distributions of all the reported variables, without artificial discontinuities at the interface between the two layers.

Downloaded from academic.oup.com/jom/article/doi/10.1093/jom/ufag025/8845483 by Politecnico di Torino user on 30 September 2026

Table 17 Benchmark B4, simply-supported multilayered spherical shell in sensor closed circuit configuration ($\bar{P}_{z_t} = 10000\,Pa$, $\bar{P}_{z_b} = 0\,Pa$, $\bar{\Phi}_t = 0\,A$, $\bar{\Phi}_b = 0\,A$, $\bar{\mathcal{M}}_t = 1.5\,kg/m^3$, $\bar{\mathcal{M}}_b = 0.5\,kg/m^3$).

R_α/h	2	4	10	50	100
		$v\,[10^{-4}\,m]$ $(\tilde{z}/h = 0.75)$			
	−1.3878	−1.4093	−0.6084	0.2257	0.5481
		$w\,[10^{-4}\,m]$ $(\tilde{z}/h = 0.50)$			
	2.2074	4.3665	7.7076	9.4795	10.532
		$\phi\,[10^4\,A]$ $(\tilde{z}/h = 0.75)$			
	5.3009	5.4227	0.9475	−0.5564	−0.3346
		$\mathcal{M}\,[kg/m^3]$ $(\tilde{z}/h = 0.50)$			
	0.6177	0.8728	0.9775	0.9991	0.9998
		$\sigma_{\alpha\beta}\,[10^5\,Pa]$ $(\tilde{z}/h = 0.50)$			
	−5.5382	−5.5421	−0.2371	3.1883	5.4277
		$\sigma_{zz}\,[10^4\,Pa]$ $(\tilde{z}/h = 0.75)$			
	10.419	−0.5021	2.2275	2.6781	1.8492
		$\mathcal{D}_z\,[10^{-5}\,C/m^2]$ $(\tilde{z}/h = 1.00)$			
	−0.3145	−0.5526	−1.0542	−1.4575	−1.6498
		$g_z\,[10^{-4}\,kg/m^2]$ $(\tilde{z}/h = 1.00)$			
	−0.9768	−1.1267	−1.9839	−9.0385	−18.019

Results are obtained via the 3D-u-ϕ-$\mathcal{M}$ model. $\tilde{z}/h$ goes from 0 (bottom) to 1 (top).

Table 18 Benchmark B4, simply-supported multilayered spherical in sensor open circuit configuration ($\bar{P}_{z_t} = 10000\,Pa$, $\bar{P}_{z_b} = 0\,Pa$, $\bar{\mathcal{D}}_{z_t} = 0.001\,C/m^2$, $\bar{\mathcal{D}}_{z_b} = 0\,C/m^2$, $\bar{\mathcal{M}}_t = 1.5\,kg/m^3$, $\bar{\mathcal{M}}_b = 0.5\,kg/m^3$).

R_α/h	2	4	10	50	100
		$v\,[10^{-4}\,m]$ $(\tilde{z}/h = 0.75)$			
	−0.8834	−1.3180	−0.5362	4.6040	10.257
		$w\,[10^{-4}\,m]$ $(\tilde{z}/h = 0.50)$			
	−0.0560	1.2274	5.9653	22.288	39.518
		$\phi\,[10^7\,A]$ $(\tilde{z}/h = 0.75)$			
	−1.9380	−2.9710	−6.7295	−33.063	−66.102
		$\mathcal{M}\,[kg/m^3]$ $(\tilde{z}/h = 0.50)$			
	0.6177	0.8728	0.9775	0.9991	0.9998
		$\sigma_{\alpha\beta}\,[10^5\,Pa]$ $(\tilde{z}/h = 0.50)$			
	−4.4642	−5.9699	3.2367	47.060	95.749
		$\sigma_{zz}\,[10^4\,Pa]$ $(\tilde{z}/h = 0.75)$			
	−22.932	−15.462	−10.127	−1.1745	−0.1436
		$\mathcal{D}_z\,[10^{-4}\,C/m^2]$ $(\tilde{z}/h = 0.25)$			
	2.0732	2.5833	2.6238	2.5345	2.5179
		$g_z\,[10^{-4}\,kg/m^2]$ $(\tilde{z}/h = 1.00)$			
	−0.9768	−1.1267	−1.9839	−9.0385	−18.019

Results are obtained via the 3D-u-ϕ-$\mathcal{M}$ model. $\tilde{z}/h$ goes from 0 (bottom) to 1 (top).

4. Conclusions

A three-dimensional exact layer-wise formulation has been presented for the static HEE analysis of smart multilayered aerospace shell structures. The proposed model is based on the complete coupling among the elastic, electric, and hygrometric fields through five three-dimensional governing equations, namely the three equilibrium equations, the divergence equation for the electric displacement, and the Fick diffusion equation governing the moisture content. The governing equations are formulated in the mixed curvilinear orthogonal reference system, making the proposed approach suitable for spherical shells, cylindrical shells, cylinders, cylindrical panels, and plates. The solution strategy combines Navier harmonic expansions in the in-plane directions with the exponential matrix method along the thickness coordinate, providing an exact three-dimensional solution within the framework of the layer-wise approach.

The accuracy of the proposed formulation has been demonstrated through two assessment cases involving both flat and curved multilayered structures. The comparison with existing HEE solutions available in the literature shows a very good agreement, confirming the capability of the present model to accurately reproduce the coupled response.

After the assessment stage, four new benchmark problems have been presented by considering a 0°/90° multilayered configuration made of a HEE material. Simply-supported plates, cylinders, cylindrical panels, and spherical shells have been investigated over a wide range of thickness ratios under three different operating conditions, namely actuator, sensor closed-circuit, and sensor open-circuit configurations. The proposed benchmark results include both tabulated values and through-the-thickness distributions of the primary variables (displacements, electric potential, and moisture content) and the secondary variables (stress components, electric displacement components, and moisture flux components). The numerical results clearly illustrate the fully coupled interaction among the hygrometric, electric, and elastic fields, together with the characteristic features of multilayered smart structures, including zigzag behavior, material layer effects, and thickness effects. Furthermore, the imposed interlaminar continuity conditions and the prescribed loading boundary conditions are correctly satisfied in all the investigated cases.

The proposed three-dimensional HEE formulation provides a physically consistent framework for assessing multilayered aerospace smart structures subjected to simultaneous environmental and mechanical loading. By explicitly resolving the through-thickness diffusion of moisture and its interaction with the electrical and mechanical fields, the model provides detailed information on local stress, deformation, and coupled-field distributions that can support the analysis and design of smart structures operating in complex environmental conditions. The proposed formulation contributes to a deeper understanding of the static response of HEE aerospace structures and provides a reliable three-dimensional reference solution for future developments of both analytical and numerical multifield models. The benchmark results presented in this work may also serve as useful reference data for the validation of refined two-dimensional formulations and fully three-dimensional computational approaches devoted to coupled HEE analyses.

Conflict of interest

None declared.

Downloaded from academic.oup.com/jom/article/doi/10.1093/jom/ufag025/8845483 by Politecnico di Torino user on 30 September 2026

Author contributions

Salvatore Brischetto (Conceptualization, Methodology, Resources, Supervision, Writing – review & editing), Domenico Cesare (Data curation, Investigation, Software, Validation, Writing – original draft).

References

1. Brischetto S, Torre R. 3D hygro-elastic shell model for the analysis of composite and sandwich structures. *Composite Structures* 2022;**285**:1–20.
2. Brischetto S, Cesare D. A coupled hygro-elastic 3D model for steady-state analysis of functionally graded plates and shells. *Curved and Layered Structures* 2023;**10**(1):1–24.
3. Brauns J, Rocens K. Hygromechanics of composites with unsymmetric structure. *Composite Structures* 1994;**30**(6):1−7.
4. Huč S, Svensson S, Hozjan T. Hygro-mechanical analysis of wood subjected to constant mechanical load and varying relative humidity. *Holzforschung* 2018;**72**(10): 1–8.
5. Jain D, Mukherjee A. Three-dimensional hygromechanical analysis of fibre polymer composites: effect of boundary conditions. *Composites Part B* 2016;**90**:203–211.
6. Nguedjio LC, Pitti RM, Afoutou J, Dubois F, Blaysat B, Talla Kisito P Recho, NImpact of hygro-mechanical loading on crack initiation and propagation in orthotropic media: a numerical modeling approach. *European Journal of Mechanics / A Solids* 2026;**117**:1–15.
7. Ožbelt J, Gambarelli S, Zadran S. Coupled hygro-mechanical meso-scale analysis of long-term creep and shrinkage of concrete cylinder. *Engineering Structures* 2022;**262**:1–13.
8. O'Ceallaigh C, Sikora K, McPolin D, Harte AM. Modelling the hygro-mechanical creep behaviour of FRP reinforced timber elements. *Construction and Building Materials* 2020;**259**:1–12.
9. Steinbrecher G, Cohen B, Altus E. Hygromechanical coupling in laminate composites and its effect on interlaminar failure. *Composites: Part A* 2016;**84**:123–133.
10. Wang J, Cui W. A cross-scale hygro-mechanical coupling model for hollow glass bead/resin composite materials. *International Journal of Solids and Structures* 2023;**264**:1–13.
11. Mohamed Ali JS, Alsubari S, Aminanda Y. Hygrothermoelastic analysis of orthotropic cylindrical shells. *Latin American Journal of Solids and Structures* 2016;**13**(3):1679–7825.
12. Hirwani CK, Akkasali NK, Kumar EK, Kumar R, Mehar AK, Panda SK. Nonlinear transient analysis of delaminated composite shell panel under hygro-thermo-mechanical load and experimental validation. *Composites Part A* 2025;**189**:1–13.
13. Jouneghani FZ, Dimitri R, Tornabene F. Structural response of porous FG nanobeams under hygro-thermo-mechanical loadings. *Composites: Part B* 2018;**152**:71–78.
14. Kundu CK, Han JH. Nonlinear buckling analysis of hygrothermoelastic composite shell panels using finite element method. *Composites: Part B* 2009;**40**:313–328.
15. Mahato PK, Maiti DK. Aeroelastic analysis of smart composite structures in hygro-thermal environment. *Composite Structures* 2010;**92**:1027–1038.
16. Moleiro F, Carrera E, Li G, Cinefra M, Reddy JN. Hygro-thermo-mechanical modelling of multilayered plates: hybrid composite laminates, fibre metal laminates and sandwich plates. *Composites Part B* 2019;**177**:1–22.
17. Moleiro F, Carrera E, Ferreira AJM, Reddy JN. Hygro-thermo-mechanical modelling and analysis of multilayered plates with embedded functionally graded material layers. *Composite Strctures* 2020;**233**:1–19.
18. Monge JC, Mantari JL, Arciniega RA. 3D semi-analytical solution of hygro-thermo-mechanical multilayered doubly-curved shells. *Engineering Structures* 2022;**256**:1–18.
19. Penna R, Feo L, Lovisi G, Fabbrocino F. Hygro-thermal vibrations of porous FG nano-beams based on local/nonlocal stress gradient theory of elasticity. *Nanomaterials* 2021;**11**(4):1–16.
20. Pham QH, Tran VK, Nguyen PC. Hygro-thermal vibration of bidirectional functionally graded porous curved beams on variable elastic foundation using generalized finite element method. *Case Studies in Thermal Engineering* 2022;**40**:1–20.
21. Pham QH, Tran TT, Tran VK, Nguyen PC, Nguyen-Thoi T, Zenkour AM. Bending and hygro-thermo-mechanical vibration analysis of a functionally graded porous sandwich nanoshell resting on elastic foundation. *Mechanics of Advanced Materials and Structures* 2021;**29**(27):5885–5905.
22. Pham QH, Nhan HT, Tran VK, Zenkour AM. Hygro-thermo-mechanical vibration analysis of functionally graded porous curved nanobeams resting on elastic foundations. *Waves in Random and Complex Media* 2023;1–32, https://doi.org/10.1080/17455030.2023.2177500.
23. Rao YN, He Q, Dai HL. A micromechanical model for effective hygro-thermo-elastic properties of fiber reinforced composites with functionally graded interphases. *Applied Mathematical Modelling* 2021;**92**:78–98.
24. Rezaiee-Pajand M, Masoodi AR. Hygro-thermo-elastic nonlinear analysis of functionally graded porous composite thin and moderately thick shallow panels. *Mechanics of Advanced Materials and Structures* 2022;**29**(4):594–612.
25. Tocci Monaco G, Fantuzzi N, Fabbrocino F, Luciano R. Hygro-thermal vibrations and buckling of laminated nanoplates via nonlocal strain gradient theory. *Composite Structures* 2021;**262**:1–10.
26. Tornabene F, Viscoti M, Dimitri R. Hygro-thermo-mechanical equivalent layer-wise theory of laminated shell structures. *Computer Modeling in Engineering & Sciences* 2025;**142**(2):1697–1765.
27. Arshid E, Soleimani-Javid Z, Amir S, Dinh Duc N, Higher-order hygro-magneto-electro-thermomechanical analysis of FG-GNPs-reinforced composite cylindrical shells embedded in PEM layers. *Aerospace Science and Technology* 2013;**126**:1–19.
28. Barati AR, Shariyat M. Exact closed-form solutions for behavior investigation of heterogeneous piezo-magneto-elastic discs under magneto-electro-hygro-thermo-

Downloaded from academic.oup.com/jom/article/doi/10.1093/jom/ufag025/8845483 by Politecnico di Torino user on 30 September 2026

mechanical loads. *European Journal of Mechanics / A Solids* 2023;**101**:1–26.
29. Dini A, Abolbashari MH. Hygro-thermo-electro-elastic response of a functionally graded piezoelectric cylinder resting on an elastic foundation subjected to non-axisymmetric loads. *International Journal of Pressure Vessels and Piping* 2016;**147**:21–40.
30. Dong B, Zhao R, Yu K. Nonlinear combined harmonic resonances of composite cylindrical shells operating in hygro-thermo-electro-magneto-mechanical fields. *Composite Structures* 2024;**331**:1–33.
31. Ebrahimi F, Boreiry M, Reza Shaghaghi G. Nonlinear vibration analysis of electro-hygro-thermally actuated embedded nanobeams with various boundary conditions. *Microsystem Technologies* 2018;**24**:5037–5054.
32. Marzbanrad J, Reza Shaghaghi G, Boreiry M. Size-dependent hygro–thermo–electro–mechanical vibration analysis of functionally graded piezoelectric nanobeams resting on Winkler–Pasternak foundation undergoing preload and magnetic field. *Microsystem Technologies* 2018;**24**:1713–1731.
33. Marzbanrad J, Reza Shaghaghi G, Shaghaghi G, Boreiry M. Nonlinear vibration analysis of piezoelectric functionally graded nanobeam exposed to combined hygro-magneto-electro-thermo-mechanical loading. *Materials Research Express* 2018;**5**(7):1–26.
34. Nie B, Meng G, Ren S, Wang J, Ren Z, Zhou L, Liu P. Stable node-based smoothed radial point interpolation method for the dynamic analysis of the hygro-thermo-magneto-electro-elastic coupling problem. *Engineering Analysis with Boundary Elements*, 2022;**134**:435–452.
35. Nie B, Ren S, Li W, Zhou L, Liu C. The hygro-thermo-electro-mechanical coupling edge-based smoothed point interpolation method for the response of functionally graded piezoelectric structure under hygrothermal environment. *Engineering Analysis with Boundary Elements* 2021;**130**:29–39.
36. Nie B, Meng G, Zhou L. The static and dynamic analysis for the coupling hygro-electro-mechanical multifield problems via stabilized node-based smoothed radial point interpolation method. *Mechanics of Advanced Materials and Structures* 2022;**30**(13):2651–2667.
37. Raja S, Sinha PK, Prathap G, Dwarakanathan D. Influence of active stiffening on dynamic behaviour of piezo-hygro-thermo-elastic composite plates and shells. *Journal of Sound and Vibration* 2004;**278**:257–283.
38. Tariq MH, Younas U, Dang H, Ren J. A general solution for three dimensional steady-state transversely isotropic hygro-thermo-magneto-piezoelectric media. *Applied Mathematical Modelling* 2020;**80**:625–646.
39. Tariq MH, Dang H, Ren J. Green's functions for infinite orthotropic, hygro-electromagneto-thermoelastic materials. *Archive of Applied Mechanics* 2022;**92**:3325–3342.
40. Tornabene F, Viscoti M, Dimitri R. Equivalent layer-wise theory for the hygro-thermo-magneto-electro-elastic analysis of laminated curved shells. *Thin-Walled Structures* 2024;**198**:1–41.
41. Tornabene F, Viscoti M, Dimitri R, Rabczuk T. Hygro-thermo-electro-mechanical coupled modeling of laminated curved panels. *Thin-Walled Structures* 2025;**215**:1–49.
42. Vinyas M, Kattimani SC, Joladarashi S. Hygrothermal coupling analysis of magneto-electroelastic beams using finite element methods. *Journal of Thermal Stresses* 2018;**41**(8):1063–1079.
43. Wang Y, Li F, Nie X, Zhang J, Xu X, Ni Y. An analytical approach for free vibration of hygrothermal–electro–elastic composite cylindrical shells. *Journal of Vibration Engineering & Technologies* 2024;**12**:5893–5904.
44. Wang W, Shan X, Xie J, Li X, Shi P. Analytical solution on magneto-electro-elasto-hygrothermal coupling in rotating functionally graded piezoelectric/piezomagnetic cylinders on Winkler elastic foundation. *Mechanics Based Design of Structures and Machines* 2025;**53**:722–752.
45. Yang Y, Donga Y, Li Y. Buckling of piezoelectric sandwich microplates with arbitrary in-plane BCs rested on foundation: effect of hygro-thermo-electro-elastic field. *The European Physical Journal Plus* 2020;**135**(61):1–31.
46. Zenkour AM, Alghanmi RA. Hygro-thermo-electro-mechanical bending analysis of sandwich plates with FG core and piezoelectric faces. *Mechanics of Advanced Materials and Structure* 2021;**28**(3):282–294.
47. Zenkour AM. Hygrothermoelastic responses of inhomogeneous piezoelectric and exponentially graded cylinders. *International Journal of Pressure Vessels and Piping* 2014;**119**:8–18.
48. Zhang Z, Cui B, Chen P, Zhou L, Wu Y. Hygro-thermo-mechanical-electro coupling inhomogeneous isogeometric analysis of functionally graded piezoelectric structures under hygrothermal environment. *Computers and Mathematics with Applications* 2026;**204**:71–96.
49. Zhang Z, Cui B, Zhou L, Pei C. Hygro-mechanical-electrical coupling isogeometric analysis for piezoelectric material structures. *Modelling and Simulation in Materials Science and Engineering* 2025;**33**:1–27.
50. Zhou L, Nie B, Ren S, Żur KK, Kim J. On the hygro-thermo-electro-mechanical coupling effect on static and dynamic responses of piezoelectric beams. *Composite Structures* 2021;**259**:1–21.
51. Tornabene F. *Hygro-thermo-magneto-electro-elastic theory of anisotropic doubly-curved shells.*, Bologna, Italy: Società Editrice Esculapio, 2023.
52. Brischetto S, Cesare D. A three-dimensional layer-wise formulation for the coupled thermo-magneto-elastic analysis of multilayered composite flat and curved panels. *Journal of Composites Science* 2026;**10**(8):1–38.

Received: 3 July 2026. **Revised:** 22 August 2026. **Accepted:** 10 September 2026
© The Author(s) 2026. Published by Oxford University Press on behalf of Society of Theoretical and Applied Mechanics of the Republic of China, Taiwan. This is an Open Access article distributed under the terms of the Creative Commons Attribution License (https://creativecommons.org/licenses/by/4.0/), which permits unrestricted reuse, distribution, and reproduction in any medium, provided the original work is properly cited.

Downloaded from academic.oup.com/jom/article/doi/10.1093/jom/ufag025/8845483 by Politecnico di Torino user on 30 September 2026